Integrating Ultrasound Neuromodulation and Imaging

A System Concept for a Non-Invasive Image-Guided Vagus Nerve Stimulator

B. K. D. Koele

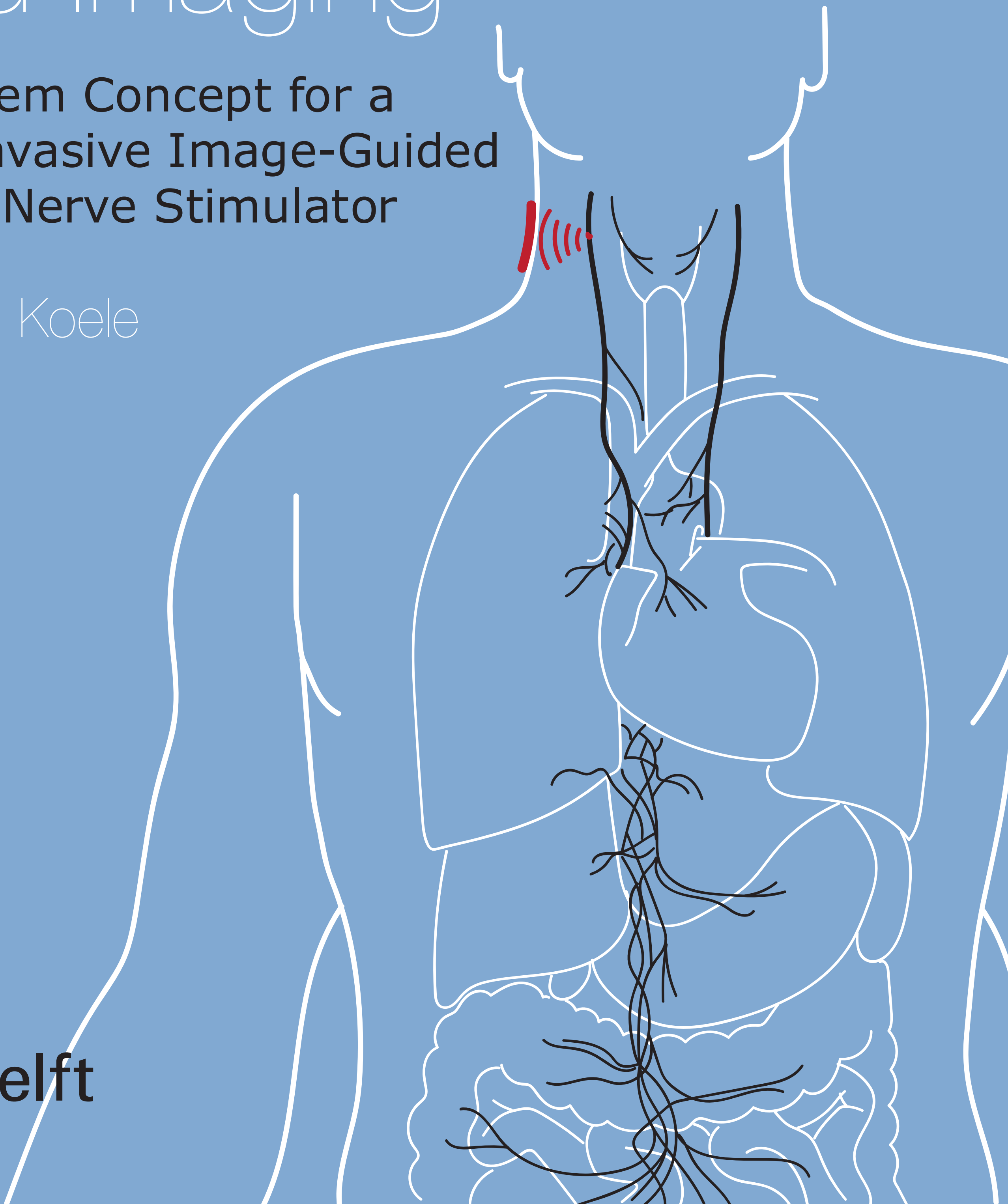

TU Delft

Integrating Ultrasound Neuromodulation and Imaging

A System Concept for a Non-Invasive Image-Guided Vagus Nerve Stimulator

by

B.K.D. Koele

to obtain the degree of Master of Science
at the Delft University of Technology,
to be defended publicly on Friday October 29, 2021 at 9:00 AM.

Student number:	4212762		
Project duration:	August 31, 2020 – October 29, 2021		
Thesis committee:	Prof. dr. ir. W. A. Serdijn,	Bioelectronics, TU Delft	Chair
	Dr. T. Costa,	Bioelectronics, TU Delft	Supervisor
	Dr. D. Cavallo,	Terahertz Sensing, TU Delft	

Cover: Envisioned wearable VNS (in red) stimulating the vagus nerve (in black). Illustration courtesy of Jill van Remundt.

Abstract

Vagus nerve stimulation (VNS) has been proven to be an effective treatment for patients suffering from drug-resistant epilepsy. Current vagus nerve stimulators are either implantable devices or bulky, handheld devices. The implant consists of a pulse generator beneath the skin of the chest, connected to electrodes that are wired to the cervical vagus nerve. While capable of delivering localized electrical impulses, the implantation is highly invasive. Handheld devices do not ask for a risky surgery, but their imprecise targeting of the neck reduces efficiency and provokes additional side effects.

Ultrasound has been widely used in clinical applications ranging from focused ultrasound (FUS) tissue ablation to medical imaging. Much research is being carried out on the use of FUS neuromodulation as a low-cost, non-invasive alternative to electrical VNS. The combination of using ultrasound for neuromodulation as well as imaging allows for image-guided FUS where automated tracking of the nerve location improves the targeting of the vagus nerve.

In this thesis, the design of an ultrasound vagus nerve stimulator with combined imaging capabilities is presented. The novel architecture combines FUS for vagus nerve neuromodulation and plane wave imaging (PWI) with optimized sparse receive sub-arrays to obtain the location of the nerve within the neck.

A 2D array of piezoelectric transducers with $\lambda/2$-pitch poses a strict constraint on the pixel area. The goal of the system design is to minimize the area consumption of the on-pixel electronics by making use of already present circuit blocks. A shared delay-locked loop generates the required continuous phases for FUS neuromodation, while a row-column pulse control block generates a single pulse from the available phases for use in PWI. This way the on-pixel transmit hardware is reduced to a multiplexer and high-voltage driver.

The receiver consists of an analog front-end and analog-to-digital converter and is shared among a sub-array of receive elements. Different degrees of random sparsity are explored for the optimal implementation of the receive sub-arrays within the full array. Synthetic aperture imaging allows the multiplexing of multiple receive elements to the shared front-end and reduces the time spent on imaging using dynamic beamforming on a single data set.

The full system-level architecture of a complementary metal-oxide-semiconductor (CMOS) interface is proposed and the receiver front-end has been designed and simulated.

List of Figures

List of Tables

List of Abbreviations

1D one-dimensional

2D two-dimensional

3D three-dimensional

A-mode amplitude-mode

ADC analog-to-digital converter

AED anti-epileptic drugs

AFE analog front-end

ASIC application specific integrated circuit

B-mode brightness-mode

BVD Butterworth-Van Dyke

CA charge amplifier

CCA common carotid artery

CMOS complementary metal-oxide-semiconductor

CMUT capacitive micromachined ultrasonic transducer

CNS central nervous system

CPA conventional phased array

CSA classic synthetic aperture

CT computer tomography

CW continuous waves

DAS delay-and-sum

DBS deep brain stimulation

DFF D flip-flop

DLL delay-locked loop

DMOS double-diffused metal-oxide-semiconductor

FDA Food and Drug Administration

FPGA field-programmable gate array

FUS focused ultrasound

HIFU highintensity focused ultrasound

HV high-voltage

IJV internal jugular vein

LNA low-noise amplifier

LV low-voltage

MRI magnetic resonance imaging

NEF noise efficiency factor

NICE neuronal intramembrane cavitation excitation

NMOS N-type metal-oxide-semiconductor

OTA operational transconductance amplifier

PET positron emission tomography

PMOS P-type metal-oxide-semiconductor

PNS peripheral nervous system

PRF pulse repetition frequency

PW pulsed wave

PWI plane wave imaging

PZT lead zirconate titanate

RMS root mean square

RX receive

SCM sternocleidomastoid

SNR signal-to-noise ratio

TGC time-gain compensation

TIA transimpedance amplifier

TMS transcranial magnetic stimulation

TX transmit

US ultrasound

VA voltage amplifier

VN vagus nerve

VNS vagus nerve stimulation

Preface

As a little boy I wanted to take apart every device to see what's inside and how it works. Sometimes I managed to put it back together afterwards. Often I did not, much to my mother's dismay. However, the choice to go to Delft has not been a difficult one.

During my time in high school, biology and medicine has never been an big interest of mine. This changed when I heard Wouter Serdijn talk about cochlear implants during one of my first lectures at the TU Delft. His passionate words triggered me to explore the field of bioelectronics. While still relatively unknown to the bigger audience, I'm sure biomedical electronics and electroceuticals will have a big impact on tomorrow's society. I'm grateful that I can say that I've contributed a tiny bit to this field.

While this document describes the results of my personal, year-long journey into ultrasound, I couldn't have done it without the help of many people. In the first place I thank my supervisor Tiago Costa for giving me guidance, but at the same time giving me the freedom to explore the many aspects of this project. His enthusiasm towards the research on ultrasound neuromodulation helped me to regain motivation in days that I questioned everything. I'm lucky to have had a supervisor who always quickly replies to questions and whose door was always open.

I would also like to thank my fellow MIND group members Hassan, Gandhi, Francesc, Ishaan, Christiaan, Bruce and Xinyu. The atmosphere during the group meetings was very pleasant and often it ended in nice conversations with interesting ideas. When I started my graduation project, the pandemic was in full swing. Working solely from home can sometimes make you feel like a one man army, but the group meetings and members helped me getting more structure.

My family has always been a great support. I'm privileged that I could always fall back to "Hotel Mum & Dad" when needed. After all these years I think I owe you a bunch of flowers. I also thank my sister Annabel, for always trying hard to stay awake when I was talking about a boring technical subject. All of you made sure to let me see there is more in life than engineering.

A big thanks to my aunt Pauline. You have always been very interested in my studies and made sure I didn't have to worry by providing me with additional financial support.

Last, but definitely not least, I couldn't have made it this far without Jill. Without you I probably still wouldn't have finished by bachelor's degree. The many days of drinking coffee in the library, listening to my complaints helped me a lot.

Now that I've concluded my time in Delft I still don't know how to put together every device. At least I can call myself engineer now.

But first: fasten your seat belt...

Berend Koele
Delft, October 22, 2021

Contents

1

Introduction

Epilepsy is a chronic brain disease that 50 million people around the world suffer from [1]. For most patients anti-epileptic drugs (AED) suffice for the suppression of epileptic seizures. However, for a group of patients the response to AEDs is too weak; they have become drug resistant against AEDs. The International League Against Epilepsy defines drug resistant epilepsy as "failure of adequate trials of two tolerated, appropriately chosen and used anti-epileptic drug schedules (...) to achieve sustained seizure freedom" [2]. This means that despite the use of carefully selected AEDs, epileptic seizures continue to exist with all imaginable consequences for individual patients.

The next step in the treatment for these patients is often electrical stimulation of the brain or the vagus nerve (VN). Deep brain stimulation (DBS) is a form of neuromodulation where electrodes are implanted into specific areas of the brain and electrical pulses stimulate the surrounding brain tissue. VNS is a similar technique where electrodes are placed near the cervical vagus nerve. Again electrical pulses are used to modulate neuronal signals. Both methods have shown to reduce the amount of seizures [3], [4]. Besides epilepsy, VNS is approved for the treatment of depression [5] and is being studied for a great number of other neurological and immunological diseases [6], [7].

Both DBS or VNS require a highly invasive procedure where electrodes have to be placed deep within the brain (in the case of DBS) or near the vagus nerve in the neck (in the case of VNS) [8]. Beside the electrodes an implantable pulse generator has to be placed inside the body.

Ultrasound (US) neuromodulation is an emerging technology that overcomes the limitations of traditional (electrical) VNS. Using ultrasound as the energy carrier for neuromodulation, no implanted electrodes are needed. This allows ultrasound to be used as a precise, but non-invasive neuromodulation modality [9], [10]. The use of ultrasound also makes it possible to combine neuromodulation with US imaging. The image can be used to locate the vagus nerve.

This project is part of a long-term vision of developing a wearable ultrasonic vagus nerve stimulator and imager. The wearable will be a patch positioned on the skin of the neck. The cover page image illustrated the wearable stimulation principle. This work is a continuation of earlier work on the CMOS design of an ultrasound transmitter and receiver channel [11], [12]. In this thesis, the system-level design of an application specific integrated circuit (ASIC) for focused ultrasound neuromodulation and imaging is described. The envisioned wearable will be able to apply image-guided VNS for optimal focusing at the nerve location.

1.1. Vagus Nerve Anatomy

The human nervous system can be divided into the central nervous system (CNS) and peripheral nervous system (PNS). The brain and the spinal cord make up the CNS, while all other nervous tissue makes up the PNS. The nerves of the PNS can be thought of as the link between the brain and the rest of the body. Like all nerves, the vagus nerve consists of bundles of individual nerve cells (neurons) with nerve fibers (axons). A neuron is an excitable cell that conducts electrical nerve impulses. An impulse is generated when the membrane voltage of the neuron is depolarized to a certain threshold. When this threshold is reached, the membrane voltage undergoes a rapid depolarization and repolarization. This nerve impulse is the action potential and it can propagate along the nerve fiber as an information

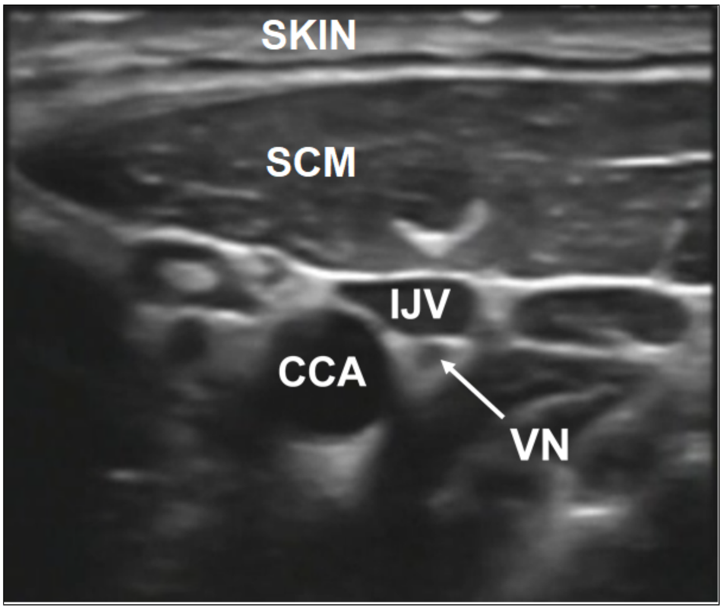

Figure 1.1: Ultrasonograph taken in the transverse plane of the left side of the human neck. The internal jugular vein (IJV), common carotid artery (CCA) and the vagus nerve (VN) can be seen below the sternocleidomastoid (SCM) muscle and the skin. Picture adapted from [14].

signal. When a nerve transports sensory information from the periphery of the body to the brain, it is called an *afferent* nerve. The other way around, when information is sent from the brain to the rest of the body, is done with *efferent* nerves. The vagus nerve can be seen as a mixed nerve, consisting of 80% afferent and 20% efferent fibres.

The vagus nerve is the tenth cranial nerve (CN X) and arises from the *medulla oblongata* in the lower brain stem. While the cell body of each neuron is located in the medulla, the axons can be very long. The vagus nerve is the longest nerve of the autonomic nervous system (a division of the PNS that regulates autonomic reflexes such as breathing, heart rate and bowel movement) and innervates almost all organs in the abdomen. This explains the Latin translation of the word vagus: *wandering*.

In the neck, the vagus nerve runs between the internal jugular vein (IJV) and the common carotid artery (CCA), surrounded by the carotid sheath. Superficial to the carotid sheath is the sternocleidomastoid (SCM) muscle, which is responsible for the rotation and flexion of the neck. An example of an image containing the vagus nerve together with the CCA and the IJV can be seen in Figure 1.1. Since the vagus nerve,CCA and IJV maintain the same relative positions within the neck, identification of any of these structures clarifies the location of the others [13].

1.2. State-of-the-art in Imaging and Neuromodulation

For decades various imaging methods have been used to obtain diagnostic information from the body without needing physical access to the internal tissue. Also, various stimulation techniques have been used to alter neuronal signals. In this section both ultrasound imaging and neuromodulation will be compared with other modalities.

1.2.1. Medical Imaging Modalities

The most common medical imaging techniques used besides ultrasound are magnetic resonance imaging (MRI), computer tomography (CT), X-ray and positron emission tomography (PET). Compared with the bulky equipment used in MRI and CT, the health issues related to ionizing radiation and the difficulty for real-time imaging make US imaging a high valued imaging modality. The use of 2D-arrays allows for accurate and automated focusing and beamforming in all dimensions, which allows for 2D or three-dimensional (3D) images to be obtained.

1.2.2. Neuromodulation Modalities

Electrical stimulation is the most common technique to alter neuronal signals. Deep brain stimulation and vagus nerve stimulation have already been discussed, but more techniques exist for the treatment of neurological disorders. Transcranial magnetic stimulation (TMS) is a non-invasive technique to stimulate the brain using rapid changing magnetic fields. Inside the brain, the magnetic field induces currents that can trigger action potentials in the neurons. It has been shown that TMS can be used in the treatment of severe headaches and depression [15], [16]. Other forms of transcranial brain stimulation modalities are direct-current (tDCS) and alternating-current (tACS) stimulation. Many other variants exist that are currently being investigated for use in medical treatments. A hand-held non-invasive electrical VNS is already available, but the bulky nature of the device and imprecise targeting does not make it long-term solution [17].

In [18], tissue displacement imaging is combined with high-intensity focused ultrasound (HIFU) for *in-vivo* research. However, the system is composed out of separate highintensity focused ultrasound (HIFU) and imaging transducers, which makes it unsuitable for wearable applications. The integration of imaging with modulation on a flexible patch has been done in [19]. While the dimensions are suited for use as a wearable, the devices still consists of two separate arrays with different transmit frequencies. The 1.3 MHz resonance frequency for neuromodulation is not sufficient for sub-millimeter spatial resolution.

1.3. Biomechanisms of Ultrasound Neuromodulation

While the effects of ultrasound on neurons are known for decades, the exact working principle of ultrasound neuromodulation is still under debate. In 1929 it was observed that ultrasound on heart cells resulted in an increased heart rate [20]. However, there was not much academic interest in this research topic. Only in the 1970s, Gavrilov et al. made considerable contributions to understanding the effects and parameters of US on peripheral nerves [21]. Recently more research is done to understand the mechanisms involved in US neuromodulation. It was shown that mechanical mechanisms are the primary source of neuron excitation via mechanosensitive ion channels in the cell membrane [22]–[24]. Other possible theories of US induced effects are the neuronal intramembrane cavitation excitation (NICE) model [25] and capacitive modulation due to membrane deformations [26]. In all cases, however, a mechanical input in the form of an acoustic radiation force seems the most promising hypothesis for US neuromodulation [22], [27].

1.4. Thesis Organization

The goal of this research was to create of system design for the integration of ultrasound neuromodulation and imaging on a single integrated circuit. The different chapters of this thesis will lead up to a created design concept.

Chapter 2 describes the underlying principles of ultrasound for medical applications. It also explains the differences between ultrasound for neuromodulation and imaging.

Chapter 4 will explore the vast possibilities of implementing 2D-arrays for imaging and neuromodulation applications. It will form a design space for the design of the system.

Chapter 4 uses the obtained knowledge to come up with a system architecture and pixel implementation for the ultrasound VNS.

Chapter 5 describes the CMOS design of the front-end amplifier, to be used in the receiver channel for ultrasound imaging.

Finally, the thesis will be concluded in Chapter 6 and future recommendations will be made.

2

Medical Ultrasound

Ultrasound is an acoustic wave, just like regular sound that humans can hear. The human ear is sensitive to acoustic waves that reach the eardrum with frequencies ranging up to 20 kHz. Ultrasound consists of sound waves above the human audible range. While ultrasound is a general physical phenomenon, medical ultrasound is often used to describe the use of ultrasound in various kinds of medical applications ranging from imaging to tissue ablation.

In this chapter, the physical mechanisms and properties of ultrasound will be given. This is necessary to obtain a good understanding of the design parameters and trade-offs in Chapter 4.

2.1. The Physics of Ultrasound

Medical ultrasound uses frequencies above the human hearing range, with a typical frequency ranging from 1 ∼ 15 MHz. Human tissue serves as the medium through which the ultrasound waves propagate. Each tissue type has its own corresponding sound velocity, but 1540 m/s is taken as a typical value. The resolution of an ultrasound image is related to the wavelength of the acoustic waves in tissue. Average wavelengths range from $0.3 < \lambda < 3$ mm [28].

For imaging, medical ultrasound uses the differences in acoustic impedance of human tissue to obtain echoes of ultrasound waves. The strength and time delays of the echoes are used to generate an image of the tissue. Human tissue is not a homogeneous material. The body consists of various tissue types like muscle, bone, liver, fat and blood. Each tissue has its specific material properties. The two properties related to ultrasound imaging are the mass density and sound velocity. Multiplied together, they form the acoustic impedance of the tissue

$$Z = \rho c \tag{2.1}$$

with Z the specific acoustic impedance [Rayls], ρ the mass density [kg/m^3] and c the speed of sound [m/s]. The properties of several types of tissue can be seen in Table 2.1.

While the different tissue properties are very similar, significant reflections occur at the boundary of two materials. This is due to the definition of the reflection coefficient, where small differences in medium properties can result in large reflections. The reflection coefficient is defined as

$$R = \frac{Z_2 - Z_1}{Z_2 + Z_1} \tag{2.2}$$

with R the dimensionless reflection coefficient and Z_1, Z_2 the acoustic impedance of two adjacent tissue types. The non-zero reflection coefficient makes it possible to distinguish between different types of tissue for imaging purposes [28].

2.1.1. Bioeffect Considerations

High-power ultrasound has the capability to damage tissue. This is exploited in a HIFU treatment to ablate cancerous tumors using heat and disintegrate kidney stone with cavitation-formed microbubbles [30], [31]. However, for most applications it is unwanted to allow tissue to heat and cavitation to occur.

Table 2.1: Properties of several tissue types. Most properties differ only slightly, with bone and air being outliers. The strong reflections from these two materials shade the deeper lying tissue. Numbers obtained from [28], [29].

	ρ [kg/m^3]	c [m/s]	Z [MRayls]
Blood	1060	1584	1.68
Bone	1990	3198	6.36
Brain	1035	1562	1.62
Fat	928	1430	1.33
Muscle	1041	1580	1.66
Water	1000	1482	1.48
Air	1	343	0.0003

Two indices exist to give a relative indication of the likelihood that heating or cavitation will occur. The thermal index (TI) can be calculated with

$$TI = \frac{W_p}{W_{deg}} \tag{2.3}$$

where W_p is the transmitted acoustic power and W_{deg} the power required to raise the tissue temperature by 1 °C. The mechanical index (MI) is given by

$$MI = \frac{PNP}{\sqrt{F_r}} \tag{2.4}$$

where PNP is the peak negative pressure in [MPa] and F_r the frequency in [MHz]. The Food and Drug Administration (FDA) has set the upper threshold at $MI = 1.9$ for diagnostic imaging.

The acoustic pressure is often translated into the more conventional wave intensity (in [W/cm^2]). The following relationship can be used:

$$I = \frac{p^2}{2\rho c} \tag{2.5}$$

with I the intensity (in W/m2), p the pressure, ρ the mass density [and c the sound velocity. In Figure 2.1, different classifications to describe intensity are given. Both spatial and temporal components of the pressure wave intensity can be used. Besides this, both the peak and average value can be given.

2.2. Ultrasound Imaging

As mentioned in the previous section, US imaging is based on the reception of reflection that arise from the boundary of different tissue types. The larger the difference is, the higher the reflection coefficient will be. This immediately leads to a shortcoming of ultrasound imaging: shadowing. A strong shallow reflector will reflect a large amount of energy. Little energy is left to reach the deeper lying tissue, leading to a low contrast image.

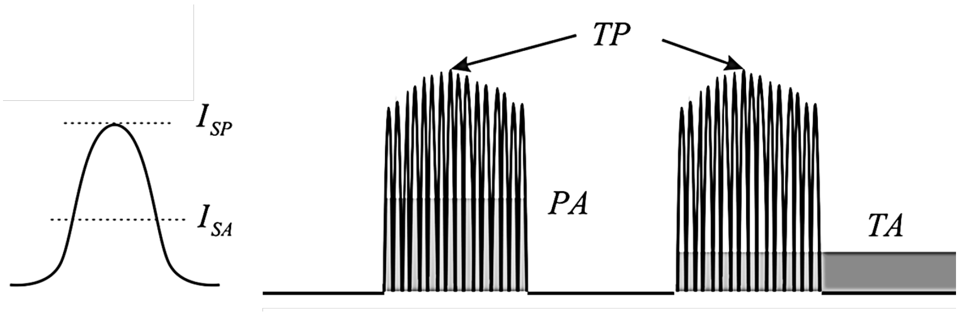

Figure 2.1: Different classifications for ultrasound intensity. SP: spatial peak, SA: spatial average, TP: temporal peak, TA: temporal average. Image obtained and adapted from [10].

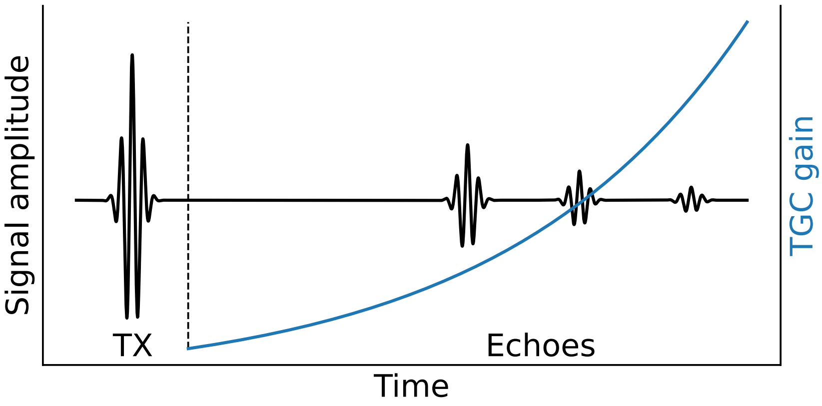

Figure 2.2: Transmitted pulse wave with corresponding echo signal. The signal becomes weaker as the wave propagates deeper into the body. In blue the ideal time-gain compensation (TGC) gain is shown. The exponential decay in echo amplitude will be compensated by an exponentially increasing gain.

In the early days of ultrasound imaging only a single transducer was used to scan the body. If the amplitude of the received signal is plotted as a function of time (which corresponds to depth), an amplitude, or *A-mode* scan is obtained. Later, multiple elements were positioned in an array. From each element a scan line is acquired. When these lines are combined to an image and the amplitude of the signal corresponds to brightness, a *B-mode* image is obtained.

From a linear (or 1D) array, a two dimensional image can be acquired. It is possible to extend this principle and obtain a 3D ‘image’ from a 2D array. In this case it is possible to image a complete volume and use 3D rendering capabilities to view the volume from all directions [32].

2.2.1. Tissue Attenuation

Once a transmitted acoustic wave enters the body, the signal will decay with time and depth. This is due to two mechanisms. First, the lossy properties of the human tissue will cause the acoustic energy in the wave to be converted into heat. This means that the power of the echo signal will reduce the longer and deeper the wave travels through the tissue. Second, since the boundary between two types of tissues is not an ideal mirror-like interface, waves will be scattered in all directions. Only a small portion of the incoming wave will be reflected back to the receive elements in the transducer. Absorption usually contributes more to tissue attenuation then scattering does [28, p.85]

The attenuation of wave is a non-linear mechanism, but it mainly depends on depth (which is proportional to time due to a near constant sound velocity), frequency and the tissue type. Typically, the attenuation factor is in the order of 1 dB/(MHz cm) [33]. Notice that the attenuation increases exponentially. A doubling in imaging depth does not attenuate the signal by two, but by four. The noise floor of the imaging system will therefore determine the maximum penetration depth that can be imaged at a certain frequency.

A time-gain compensation amplifier can be used to compensate the attenuation over time. Echoes from nearby tissue are less attenuated than echoes from deep tissue, see Figure 2.2. The former needs therefore little compensation, while the latter requires a high amplification to boost the signal to appropriate levels for further processing. The gain of the amplifier ideally looks like an exponential function, to perfectly compensate the loss in signal amplitude from the echo. This can be seen as the blue trace in Figure 2.2.

2.3. Transducers

In order to transmit pulses and receive their echoes, a transducer is needed that can convert electrical signals to sound waves and back. Piezoelectric materials are commonly used as the transducer material in ultrasound probes. The piezoelectric effect is a phenomenon in which materials exhibiting the effect can generate an internal charge difference under an applied force. The effect is reversible, meaning that a mechanical strain is generated from an applied electric field.

Piezoelectric materials can be characterized with the electromechanical coupling coefficient k_{33}. This coefficient can be seen as the transducer efficiency, since it is the ratio of mechanical output power to electrical input power. The subscript indicates the direction of polarization and mechanical strain. Commonly, lead-based ceramic materials are used as piezoelectric material. One of the most widely used compounds is the lead zirconate titanate (PZT) ceramic. This is a perovskite material with the chemical formula $Pb[Zr_xTi_{1-x}]O_3$ $(0 \leq x \leq 1)$. Its high electromechanical coupling coefficient (k_{33} = 0.75) make it an efficient transducer. Another material that attracted attention more recently is PMN-PT (a single $Pb(Mg_{1/3}Nb_{2/3})O_3$-$PbTiO_3$ crystal). It has an even higher coupling coefficient of $k_{33} \approx 0.92$ which makes it a suitable material for use in low amplitude echo receivers [12]. However, PMN-PT is a very brittle material which makes it difficult to work with.

In this work, the use of the piezoelectric material PZT-5H is assumed. The parameters of this material will be used to create a lumped-element model. The datasheet can be found in [34] and some properties are listed in Table 2.2.

The electromechanical coupling coefficient can be described by

$$k_{33} = \sqrt{\frac{\pi}{2}\frac{F_r}{F_a}\tan\left(\frac{\pi}{2}\frac{F_a - F_r}{F_a}\right)} \tag{2.6}$$

with F_r and F_a the resonance and anti-resonance frequency, respectively. Improving k_{33} can lead to an increase of the bandwidth of the transducer [35]. Often the *effective* coupling coefficient $k_{eff}^2 = \frac{F_a^2 - F_r^2}{F_a^2}$ is used in equations. Usually k_{eff} is slightly lower than k_{33}.

A piece of piezoelectric material has multiple resonance modes. The dominance of each mode is determined by the geometry of the material. If the dimension parallel to the poling direction is the thickness t and both lateral (perpendicular) dimensions along the poling surface are L (assuming a square surface), the aspect ratio $G = L/t$ can be defined. For thin bar geometry, $G \ll 1$ and the length-extension (LE) vibration mode is used. If $G \gg 1$, the width-expansion (WE) vibration mode is dominant [36]. The fundamental resonance frequency corresponds to the $\lambda/2$.

The geometry of the piezoelectric material determines the resonance frequency and vibration mode of the transducer. Each dimension has an associated half-wavelength fundamental resonance frequency. In the case of a bar-shaped transducer (see Figure 2.3) with a thickness much greater than the lateral dimensions, the thickness-mode resonance frequency dominates [28].

For LE-resonating transducers, the resonance frequencies can be calculated by

$$f_p = c_{piezo}/2T \tag{2.7}$$

$$f_s = f_p\sqrt{1 - k_{eff}^2} \tag{2.8}$$

Another type of transducer that is common nowadays are capacitive micromachined ultrasonic transducer (CMUT)s. These transducers work electrostatically and do not use the piezoelectric effect. The device consists of a flexible membrane and a fixed substrate material acting as two plates of a capacitor. By superimposing an alternating signal on top of a fixed bias voltage, the membrane will vibrate and generate pressure waves. Advantages of CMUTs over piezoelectric transducers are the wide bandwidth (low quality-factor) and the fact that conventional planar fabrication techniques can be used [37].

Table 2.2: Some material properties of PZT-5H from [34].

Property	Symbol	Value	Unit
Coupling Coefficient	k_{33}	0.75	-
Dielectric Constant	K_3^T	3800	-
Density	ρ	7870	kg/m^3
Charge Coefficient	d_{33}	650	pC/N
Elastic Constant	s_{33}^D	8.8	pm^2/N

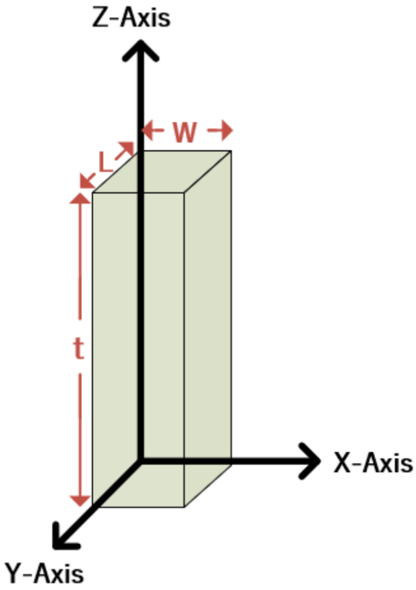

Figure 2.3: Bar-shaped piezo material exhibiting length-extension vibration mode. The thickness t is much larger than the width W and length L.

2.3.1. Lumped-element Model

In Figure 2.4 the Butterworth-Van Dyke (BVD) lumped-element model of a piezoelectric transducer is shown. The series RLC circuit is called the motion branch since it models the mechanical properties of the material. The parallel capacitor C_p is due to the electrical properties of the transducer.

The inductance L_s is due to the inertia of the piezoelectric material, the capacitance C_s is due to the elasticity (stiffness) of the device and resistance R_s represents the lossy nature of the material.

The model has a resonance and anti-resonance frequency f_r and f_a, respectively. The equivalent impedance of the model is at a minimum during resonance and at a (local) maximum during anti-resonance. At resonance, the impedance of the motion branch drops to R_s, since the series inductance L_s and capacitance C_s cancel each other. The resonance frequency can be given by $F_r = 1/2\pi\sqrt{L_s C_s}$.

2.4. Differences between Neuromodulation and Imaging

Although US imaging and neuromodulation are very similar techniques, there are differences in the design of each system. Of course, for neuromodulation no echo reception is needed, thus eliminating the need for a receiver. For transmission, however, there are also some differences. The ultrasound intensity at the focal spot is directly related to the neuromodulation effects. The intensity should be high and the focal spot small. This has consequences for the array design. Also the short pulsed wave required for imaging and the continuous waves required for neuromodulation poses some design trade-offs.

2.4.1. Timing and Pulse Durations

Imaging relies on the transmission of a short pulse and the reception of the corresponding echo. The duration of the echo is proportional to the depth of the scattering object within the body. A consequence of this is that the imaging frame rate is determined by the time of flight of the pulse. The round-trip time T_{RT} that the pulse is propagating is $T_{RT} = 2z_{max}/c_0$, with z_{max} the imaging depth and c the speed of sound. For the highest frame rate, the pulse repetition frequency (PRF), shown in (2.9), should be the inverse of the round trip time. This means that no additional time is spent on computations or configurations between the pulse transmissions [38]. The overall frame rate of the imaging system is not only determined by the PRF, but also by the number of scans required to obtain an image.

$$PRF = \frac{1}{T_{RT}} = \frac{c}{2z_{max}} \tag{2.9}$$

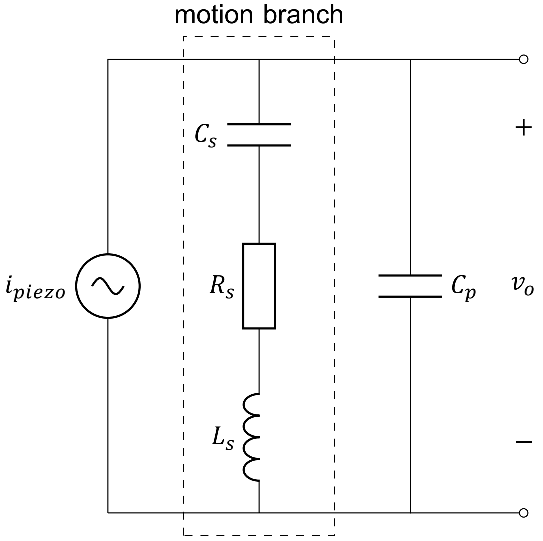

Figure 2.4: Butterworth-Van Dyke model of the piezoelectric transducer.

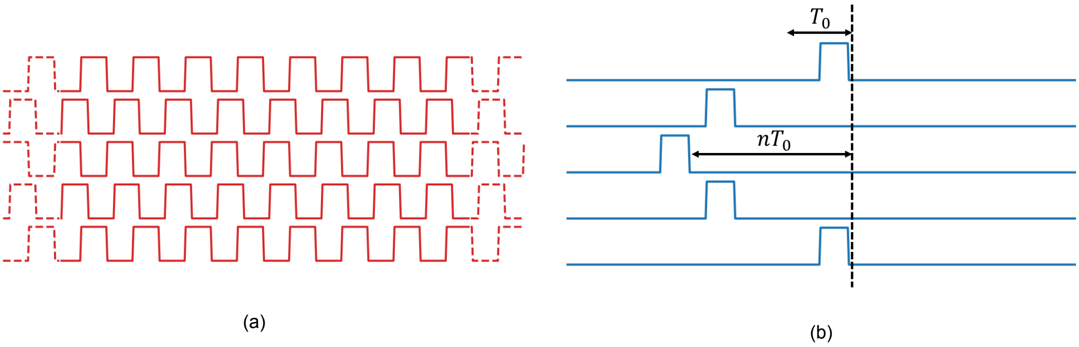

(a)

(b)

Figure 2.5: Continuous waves for neuromodulation (a) and pulsed waves for imaging with delays of multiple periods T_0 (b).

According to (2.9), the maximum PRF for a depth of e.g. 10 cm is 7.5 kHz.

$$DC = PD \times PRF \times 100\% \tag{2.10}$$

For neuromodulation short pulses are not enough to transmit enough acoustic energy to the neurons in order to generate action potentials. The duty cycle (DC) is the ratio of the pulse duration (PD) and the pulse repetition period (see (2.10)). Where for imaging the duty cycle is usually very low (DC $\leq 2\%$), it can be up to 100% for neuromodulation [10]. Pulse durations for imaging are often only a couple of cycles, which is in the order of microseconds. For neuromodulation, the pulse duration can last hundreds of milliseconds. This limits the PRF to tens of hertz.

The difference in continuous wave for neuromodulation and pulsed waves for imaging also requires a different phase generation. The continuous nature allows the phases to wrap to a $[0, 2\pi)$ interval. The maximum delay is therefore no longer than one period. For imaging this is different. Since only a single pulse is transmitted, the maximum delays can reach multiple (> 10) time periods [11], see Figure 2.5. This will only increase when the array size grows.

2.4.2. Acoustic Intensity

The intensity calculated in Section 2.1.1 can be used as a metric to compare the powers required for imaging and neuromodulation. The spatial-peak temporal-average intensity I_{SPTA} for imaging is usually below 1 W/cm^2 [28]. To elicit neuronal responses for neuromodulation, high enough pressures are required to reach the action potential threshold. It has been shown that nerves in the PNS also require higher intensities than CNS nerves. This may be due to the nerve myelination and axonal bundle sizes. Nominal pressures for PNS neuromodulation are in the order of 1 MPa and higher [39].

It has been shown that intensities of $I_{SPTA} \leq 200\,\mathrm{W/cm^2}$ elicit radiation force induced neuromodulation [10]. At even higher intensities, thermal and cavitation induced effects occur, which might lead to tissue damage.

2.4.3. Transducer Design

The different waveforms for both applications also pose a trade-off in the design of the transducer elements. Ideally, a perfect (delta) impulse is transmitted for imaging so that the echo signal scattered from different types of tissue perfectly describes the tissue. Mathematically this can be seen as obtaining the spatial impulse response of the tissue. The axial resolution of an ultrasound image is proportional to the bandwidth of the transmitted signal. Since the electrical excitation is converted to a pressure wave via the transducer elements (i.e. the electrical pulse is convoluted with the transducer's impulse response), the bandwidth of the transducer also plays a role in the image resolution. For a high-resolution image, a short pulse wave should be transmitted with a high-bandwidth transducer. This means that the quality factor $Q = F_r/BW$ of the transducer should be low [28].

The disadvantage of a low-Q transducer is the fact that energy efficient transmission at resonance is not possible. While this might not be a problem for the PW transmission used in imaging, it poses a problem when long pulse durations are used in neuromodulation. The CW nature would benefit from a high-Q transducer, so that little energy is required for excitation.

2.4.4. Array Design

As discussed in the previous sections, the ultrasound intensity is directly related to the neuromodulation effects. Long pulse durations with high intensities are needed to elicit neuronal responses. To reach the required intensities in a small spatial focal spot, a 2D array is needed since focusing can be done in both lateral planes. The large number of transducers in a 2D array allows for a high acoustic pressure at the focal spot. On the other hand, a linear array is usually sufficient to produce a regular image. A linear array also means that focusing can only be done in the lateral dimension of the array. A fixed elevation beam width is determined by the length of the elements.

3

Phased Arrays and Beamforming

In this chapter various ways of using arrays of ultrasound transducers will be discussed. First the classic implementation of ultrasound imaging using phased arrays and fixed transmit focusing will be discussed. Then, the application of more modern imaging schemes will be discussed. This will form the basis for the design of the combined ultrasound neuromodulation and imaging system. The design concept will be explained in Chapter 4.

3.1. Conventional Phased Arrays

An important feature of linear or 2D arrays is the ability to focus and steer waves in a specific direction. While every individual transducer element emits a spherical wave (i.e. energy is transmitted in every direction), the wavefront of the combined array can be steered and focused by applying phase differences in the excitation of individual elements. This phenomenon can be seen as a form of diffraction because each elements' wavefront is superimposed on every other wavefront, thus creating areas of constructive and destructive interference. The phase of the transmit signal is changed for each transducer element, which results in the steering and focusing of the beam to a narrow focal spot. As an example, two delay profiles are generated using the delay equations from [40] for 2D-arrays. The profiles can be seen in Figure 3.4. A higher value means a longer delay with respect to the lower values.

The dimensions of the 2D array are an important design parameter. It can be seen in Figure 3.1 that the lateral distance between transducers, the pitch p, determines the phase difference for a given steering angle θ,

$$\Delta x = p \sin\theta \tag{3.1}$$

For a focused beam, the steering angle for each transducer is slightly different. However, since the focus depth is usually much larger than the pitch, the angles between subsequent elements do not

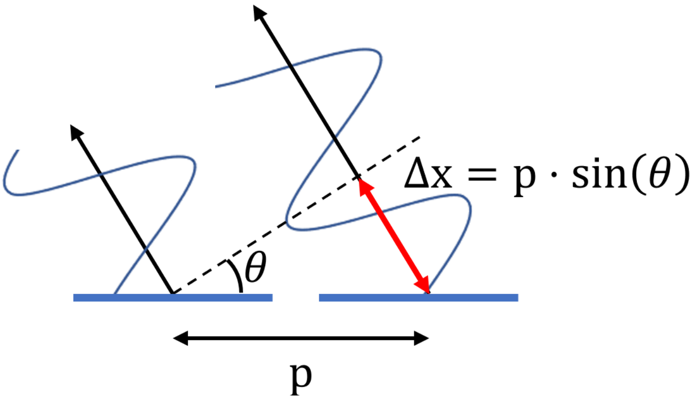

Figure 3.1: A periodic array of transducers will exhibit diffraction patterns due to the phase differences between individual elements. For a given steering angle θ and pitch p the phase difference Δx can be calculated.

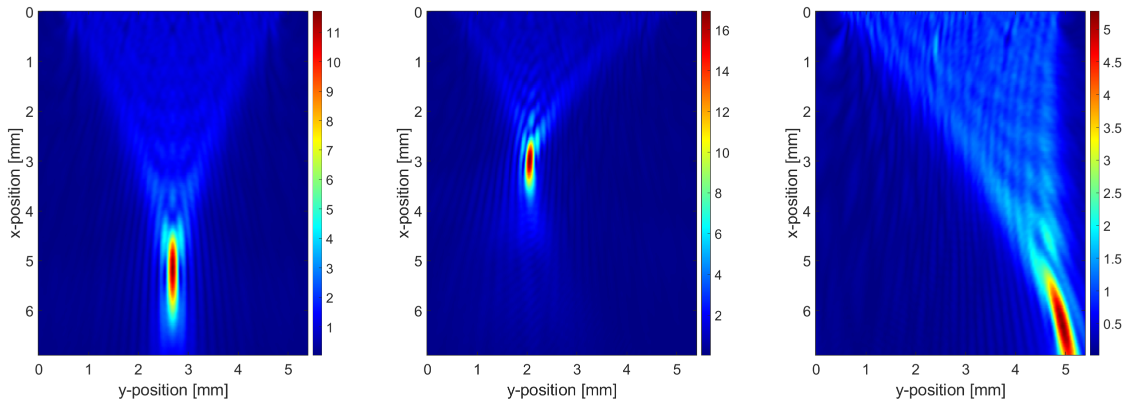

(a) (b) (c)

Figure 3.2: Focused ultrasound creating a high-intensity focal spot at different locations in the image plane.

change significantly.

Besides the wanted beam, grating lobes can occur at different angles due to the finite and periodic nature of the array. Grating lobes occur at angles θ_g where the phase difference is an integer multiple of the wavelength, or $\Delta x = m\lambda$. Rewriting (3.1) gives the grating lobe angle

$$\theta_g = \arcsin \frac{m\lambda}{d} \quad \text{with} \quad m = \pm 1, \pm 2, \text{etc.} \tag{3.2}$$

It can be seen that when the pitch equals one wavelength $d = \lambda$, grating lobes occur at ±90°. For a pitch $d = \lambda/2$, (3.2) has no solution[1]. Grating lobes are completely avoided when $d \leq \lambda/2$ [28].

As mentioned in Section 2.2, a linear array can used to obtain a 2D imaging. This means that the beamforming operation takes place in the image plane. For a 2D array, beamforming can be done in both lateral dimensions of the array. This means that focusing can be done in all three dimensions. For a 2D array, both dimensions need to satisfy the half-wavelength pitch requirement for the transducers to suppress grating lobes. The disadvantage is that the transducer elements become very small. The pressure generated by a single element will be small compared to the often longer elements in a linear array.

Traditionally, a B-mode image is obtained by adding scan lines obtained from transmitting a focused beam with a certain angle. By sweeping the angle, the image is obtained line by line.

Beamforming can be done in both transmission and reception. Transmit beamforming consists of applying delays to the transmit signals before transmission in order for the waves to coherently add at the focal spot. Receive beamforming works by choosing a location in the image plane and applying delays to the received signals as if a point source emits from that location. These signals are then summed to obtain a scan line in the direction of the point source. If a scattering object is located at that point, a strong echo will result from the summation over all receive (RX) channels. If not, the resulting summation will not contain a strong echo, but multiple weak echoes belonging to each channel. This RX beamforming technique is usually referred to as delay-and-sum (DAS) beamforming.

3.2. Synthetic Aperture Imaging

While conventional phased array imaging leads can lead to images with a high contrast (i.e. high signal-to-noise ratio (SNR)), there are several disadvantages. First of all, a fully sampled phased array with N transducer element requires also N transmitter and receiver channels. This can be feasible for a linear array, where there is enough silicon area to incorporate pitch-matched channels. For larger 2D-arrays, especially at higher frequencies, this will not be possible.

Instead of using all N transducer elements for both transmit and receive, it is also possible to use only a subset of the elements for transmission or reception. By changing the subset for each transmit-receive (or pulse-echo) sequence, the full aperture of the array can synthetically be generated using

---

[1] From (3.2) it can be seen that for all $d < \lambda$ there is no solution. For linear arrays, a more complete expression for grating lobe angle θ_g with a steering angle θ is $\sin\theta_g = \sin\theta + m\lambda/d, \quad m = \pm 1, \pm 2,$ etc. [40]. For small θ this reduces to (3.2).

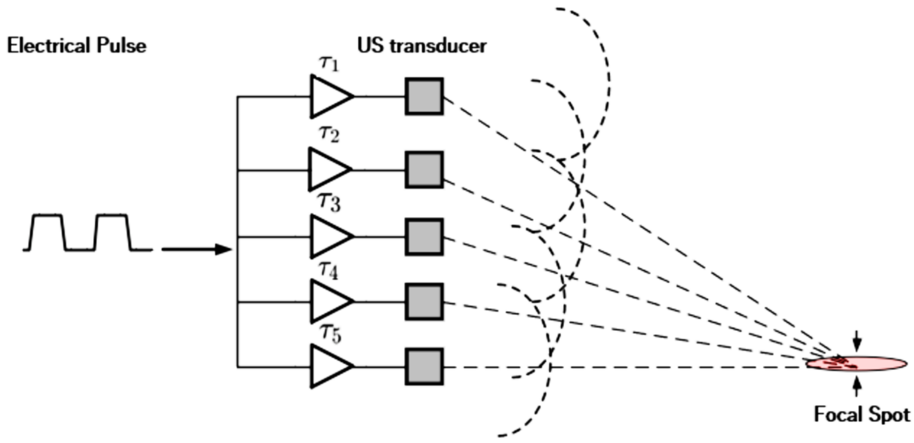

Figure 3.3: Phased array showing transmit beamforming. While each element emits a spherical wave, the summed wavefront is steered and focused into a focal spot. Image obtained from [12].

only a small number of elements. This techniques has initially been developed for *synthetic aperture radar*, where a large area (e.g. a landscape) can be imaged using a single antenna on a moving airplane.

Classic synthetic aperture (CSA) ultrasound is derived from this radar technique. Only a single transducer element of an array is used at a time as both the transmit (TX) and RX element. After each pulse-echo sequence, the adjacent element in the array is activated until the entire array aperture is synthesized. This imaging scheme is illustrated in Figure 3.5. One of the downsides of using a classic synthetic aperture scheme instead of a full phased array is the loss in SNR. Since only a single element is active at a time, $N_{TX} = 1$. In (3.8) can be seen that this degrades the beamformed signal. A single element cannot apply transmit focusing. The wavefront of the single element approximates a spherical wave and the pressure rapidly drops. This means that after each transmit-receive sequence, a low-resolution image is obtained. By coherently summing these images, a single high-resolution image can be generated.

Synthetic aperture ultrasound is not bounded by using a single element for transmit or receive. Numeral variation exist, including using a single transmit element in combination with all receive elements or every transmit element in the array but only a single receiver. In Figure 3.6, the two synthetic aperture techniques can be seen. In Figure 3.6(a), a single element of a linear array is used for the transmission of the pulse. During reception, every element receives the echo. Next, the adjacent element is used for transmission and again every element receives this echo. This continues until the complete transmit aperture is synthesized by moving a single element across the aperture. Figure 3.6(b) combines a phased array for transmitting scan lines but only a single receiver is used [41].

In [42] a transmit sub-array of N_{TX} elements is excited with individual delays to ‘defocus’ the transmit beam. This way a spherical wavefront, similar to a single element, is obtained, but with the acoustic pressure of N_{TX} elements. The same sub-array is used for the receive elements, so $N_{TX} = N_{RX}$. After every transmit-receive sequence, the sub-array is stepped across the array one element at a time. A total number of $N - N_{TX} + 1$ sequences are needed for the sub-array to synthesize the entire aperture. If only as single element is used as a sub-array ($N_{TX} = N_{RX} = 1$), this imaging scheme reduces to classic synthetic aperture imaging.

3.3. Plane Wave Imaging

Plane wave imaging is often used for its high frame rate ability. In [43], plane wave compounding is used for very high frame rate transient elastography up to 6000 frames/s. However, the ability for high frame rate imaging is not the reason for its implementation in the scope of this thesis. Since it is expected that the vagus nerve will only move slightly around its normal position, no high frame rates are needed to track its location. The nerve movement will be mostly due to breathing, heart rate (i.e. motion of the nearby carotid artery) and rotation of the neck. Since these motions are not at high velocities, a frame rate below 10 frames/s will be sufficient.

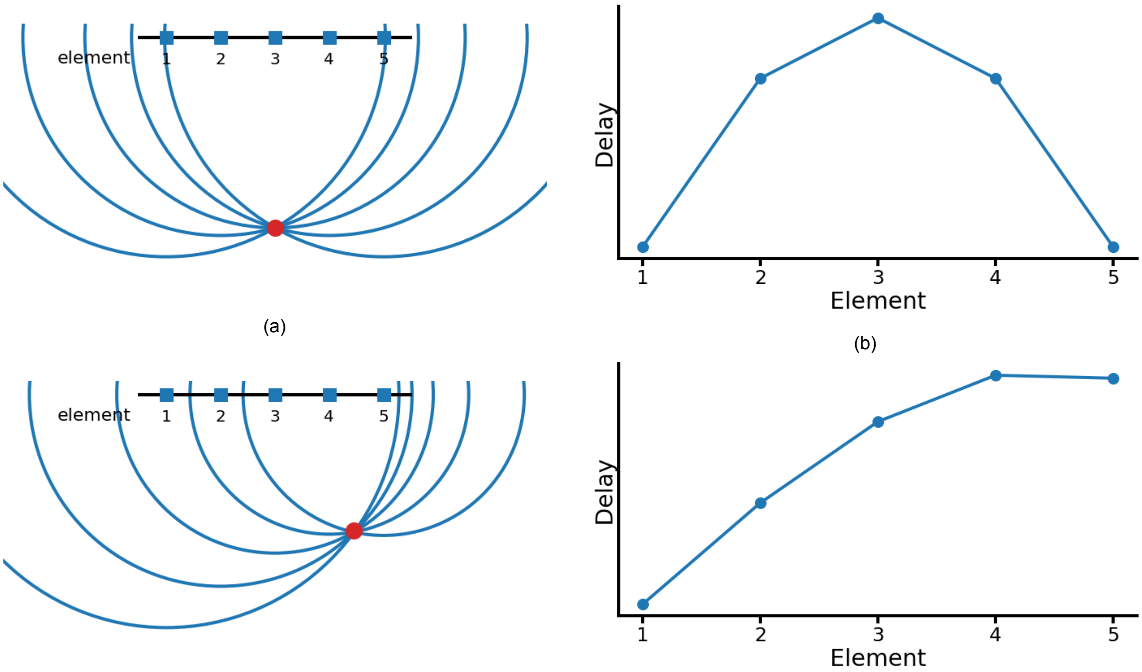

(a) (b)

(c) (d)

Figure 3.4: Phased array beamforming where different delays applied to an array of five spherical transmitters (blue squares). The transmitted waves with indicated focus spot (red dot) can be seen in (a) and (c). The delay profile for a steering angle of 0° and 30° can be seen in (b) and (b), respectively.

Montaldo et al. derive the total number of plane wave angles that are required to obtain an image without loss of information in the angular spectrum. The angles α_i can be calculated using

$$\alpha_i = \arcsin\left(\frac{i\lambda}{L}\right) \approx i\lambda/L \qquad i = -N_{TX}/2, \dots, N_{TX}-1 \tag{3.3}$$

with λ the wavelength, L the lateral dimension of the array and N_{TX} the total number of transmit elements. To generate the complete set of angles, precise phase control is required in the TX beamformer since the difference in angles is very limited. Precise phase control means the implementation of a delay-locked loop (DLL) with a high number of bits.

While the number of angles can be large, not the complete set of plane waves has to be transmitted since the directivity of the array limits the use of high spatial frequencies [44]. Less than ten plane waves can produce images that are comparable to using focused transmissions by scanning the image plane with scan lines [45].

Every aperture has its natural focusing depth at the boundary of the near-field and far-field region (for a square aperture approximately at a depth $z_n = L^2/\pi\lambda$). This is determined by the lateral dimension of the aperture L and the wavelength of the transmitted wave λ.

For PWI, the natural focusing is unwanted since a plane beam profile is used to illuminate the tissue equally at every location. Karaman et al. [42] found a way to apply delays to the array element to defocus the beam. The obtained beam profile looks similar to a spherical wavefront obtained from a single element transmission, but with higher amplitude. The mean intensity of the defocused aperture increase with the square root of the number of elements in the transmit aperture [42, fig. 1].

In Figure 3.8 the peak pressure of a plane wave transmission at two imaging depths can be seen. For a low number of columns (small aperture), the acoustic pressure increases linearly. Since the adjacent elements add coherently to the pressure, an increase is expected. On the other hand, for a large number of columns, the pressure remains constant. This can be explained by the fact that two elements far away from each other have little interaction and do not contribute to each others beam profile. The pressure behaviour for moderately sized apertures shows a peak. For a depth of 2.5 mm, the pressure is at a maximum for an aperture of 13 elements. The near-field depth for such an array is $[(13-1)\cdot 90\,\mu\text{m}]/(\pi \cdot 180\,\mu\text{m}) = 2\,\text{mm}$. This is close to the observation depth of 2.5 mm and thus

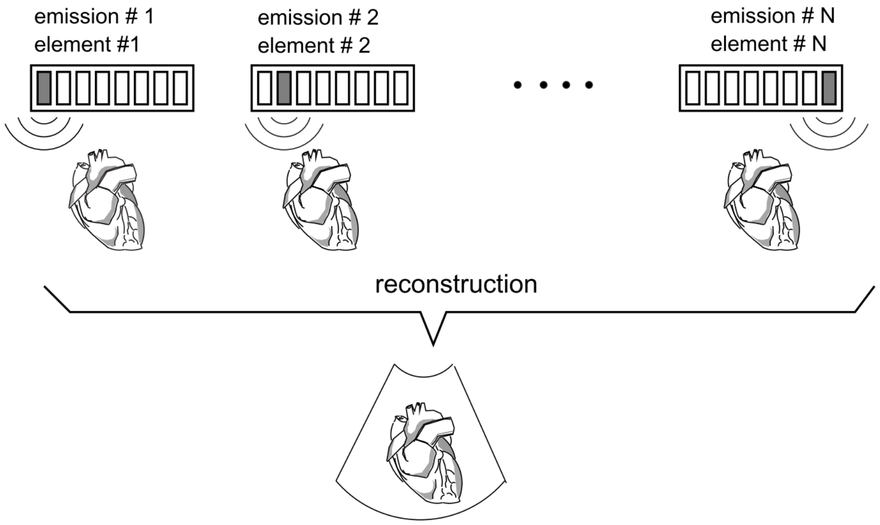

Figure 3.5: Classic synthetic aperture where one element is active at a time and stepped across the N-element array. Image from [41].

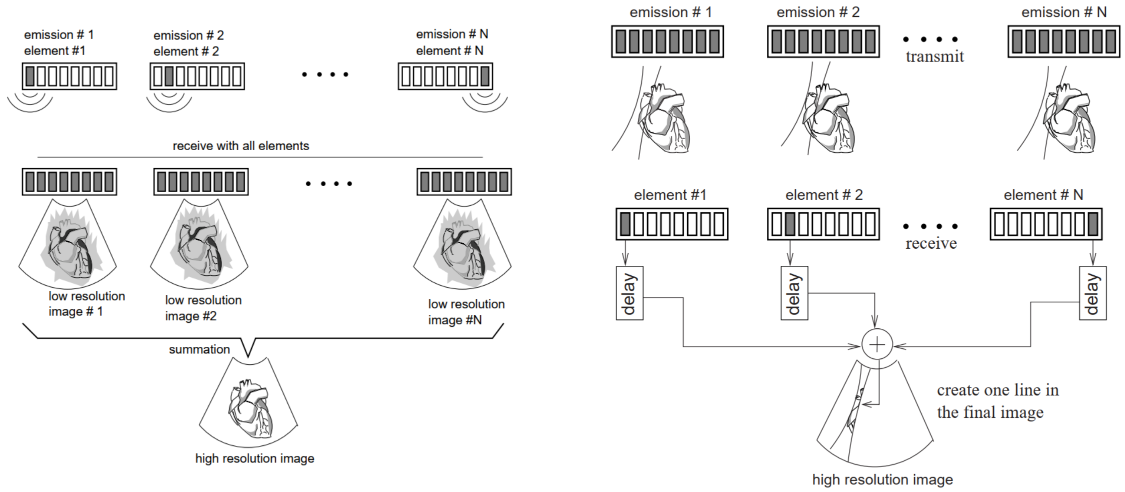

(a) (b)

Figure 3.6: Synthetic transmit aperture (a) and synthetic receive aperture (b). Image obtained from [41].

shows the natural focusing behaviour. Peaking at 5 mm depth occurs at a slightly higher aperture size, which holds with the aforementioned theory.

The beam profiles of various aperture sizes can be seen in Figure 3.9. A clear spherical wavefront is visible for the single column transmission (Fig. 3.9(a)), while the plane wavefront is visible in Fig. 3.9(i).

3.4. Sparse Arrays

When every transducer element in the array can be used for both transmit and receive, the array is fully sampled. This way the full potential of the array is used and the maximum amount of data can be extracted from it. The implementation of a fully sampled array, however, is difficult for a $\lambda/2$-pitch 2D array. The small area does not allow for a single RX and TX signal path per element. Instead, dedicated transmit elements have to be alternated with receive elements. In this section, the use of sparse arrays is described as a method to reducing the number of elements while maintaining the effective aperture of a dense, fully sampled array.

The separation of RX and TX element in its simplest form is done by in [46], where the array is

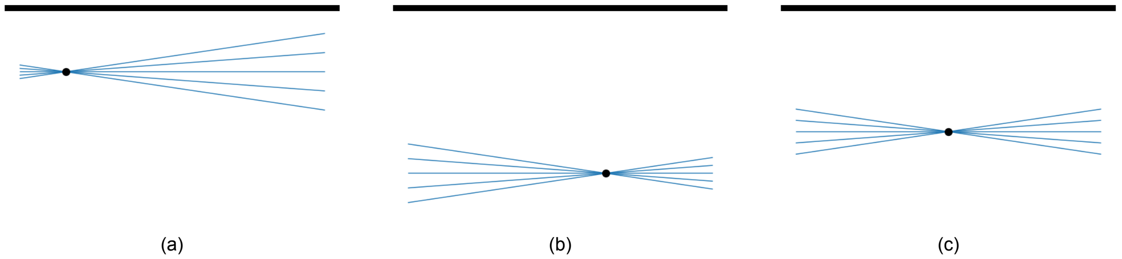

Figure 3.7: Different focus spots can synthetically be created by applying relative delays to the different angled plane wave. Five plane waves with different angles are transmitted in succession. Overlaying them results in the creation the black focal spot. The array is illustrated as the black line.

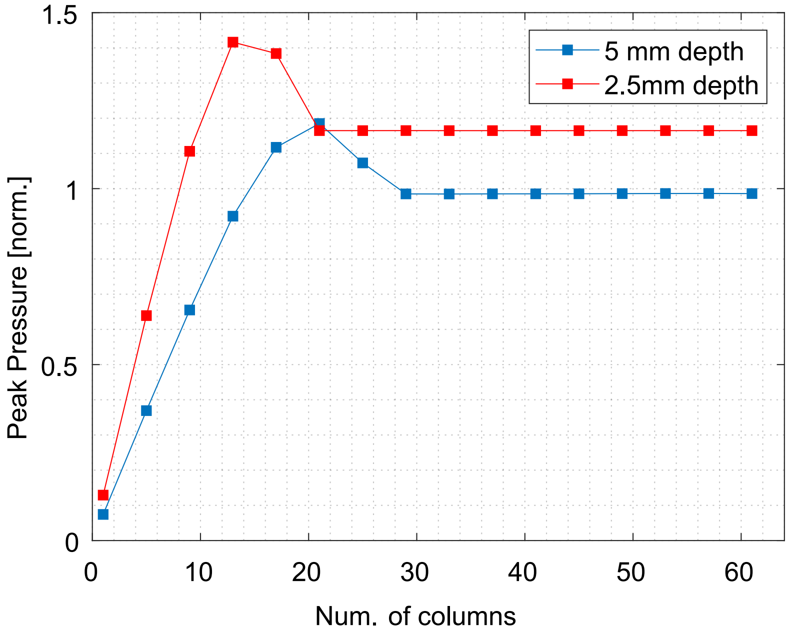

Figure 3.8: Simulation showing the peak pressures at two depths for a plane wave transmission with increasing number of columns.

divided into a rectangular TX and RX part. In a later paper, Chen et al. [47] propose a 32×32 array with a central 8×8 TX array surrounded by a majority of RX element. The opposite is done by Bhuyan et al. [48], who use an array with mostly TX elements and a cross-shaped structure of RX elements. The location of the TX and RX elements play an important role since it makes up the transmit and receive aperture. The effective aperture of the array is synthesized by the spatial convolution of the transmit and receive aperture [49]. A consequence of using elements only for reception is the change in radiation pattern for the transmit elements. To see this variation, a linear array of 64 elements is created in MATLAB (The MathWorks Inc., Natick, MA). The radiation pattern of a fully dense array is compared with one array of which 20% of the element at random locations are removed and an array of which 20% of the elements are removed in a period manner (one out of every five elements). The Fourier transform of the array gives the spatial response of the three arrays. The results can be seen in Figure 3.10. The dense array shows a radiation pattern with only a single peak, as expected. While the period sparse array shows a good directivity for small angles, high grating lobes occur at various spatial frequencies. The random sparse array does not have the highest directivity, but the random nature prevents the occurrence of grating lobes.

Scaillero and Trucco [50] use two concentric circular apertures where off-the-grid sparsity is used to optimize the array with the least number of receive elements. While a custom cost function and optimization process can improve the array design for a wanted beam profile, the fabrication of an

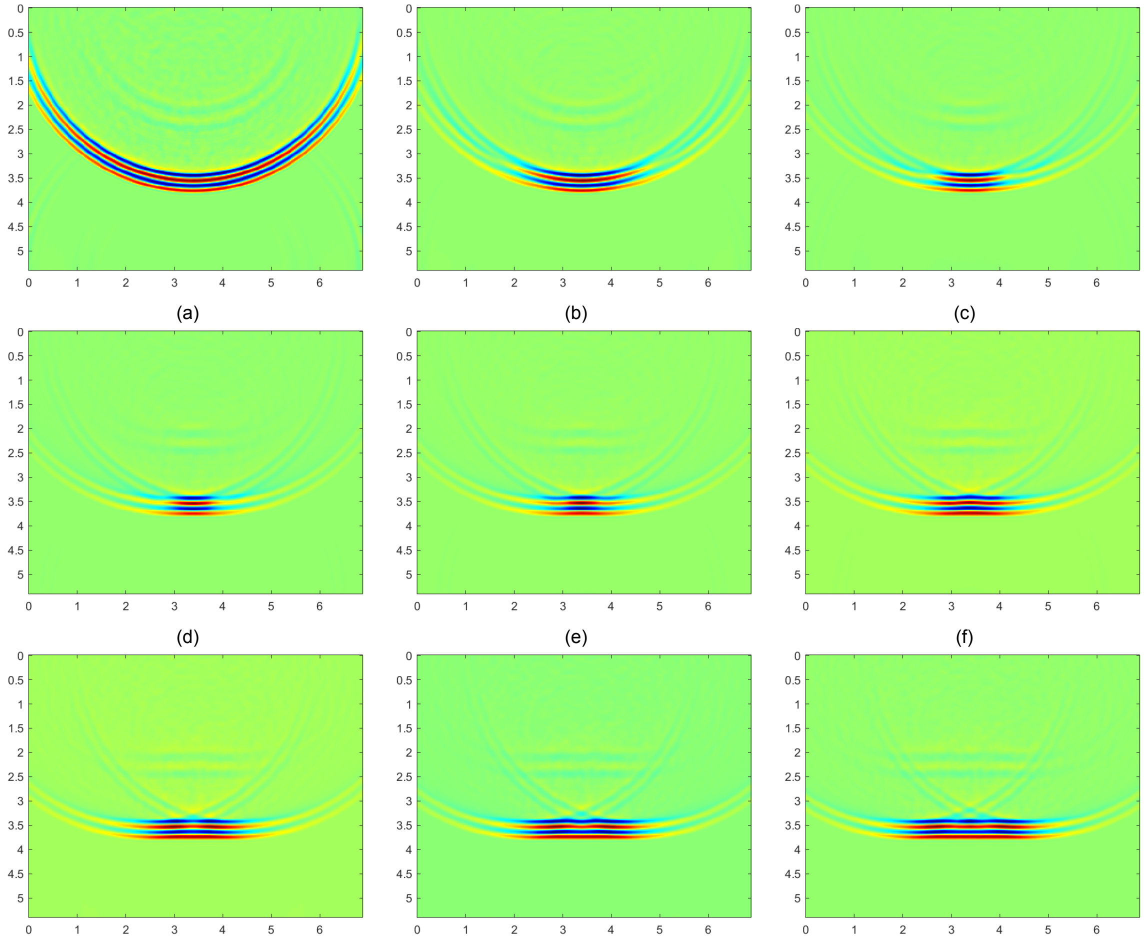

(a) (b) (c) (d) (e) (f) (g) (h) (i)

Figure 3.9: Plane-wave transmissions with various aperture sizes. The axis are in millimeters. (a) 1 column, (b) 5 columns, (c) 9 columns, (d) 13 columns, (e) 17 columns, (f) 21 columns, (g) 25 columns, (h) 29 columns, (i) 33 columns.

array without a grid structure is difficult. The same holds for the 2D-array by Lockwood [49], where an array based on vernier interpolation is implemented. This design uses different element spacing for transmit and receive and can reduce the total number of element with a factor of six compared with a dense array.

3.5. Beamforming

Once a pressure wave has entered the tissue, reflections of the incident wave will occur when there is a change in acoustic impedance. The reflections will be backscattered to the array and will be sensed by the receive elements. These elements, in combination with the receiver electronics, convert the incoming echo to an electrical signal. Beamforming is the process of combining multiple element signals into one beamformed output signal. This output signal contains echo information from a particular point on the image plane. The combining process usually consists of delaying the element signals with a calculated delay profile, followed by a summation of all element signals to obtain the output signal. If no echoes arrive from the point, only a weak, noisy signal will be left after summation [51]. This beamforming process is referred to as DAS beamforming and it is illustrated in Figure 3.11.

By changing the delay profile, one can ‘listen’ to a different location on the image plane. If at that location a reflection has arisen, a large amplitude pulse will be present in the beamformed signal because the delaying has aligned the phases of the echoes. Since the beamformed signal is a coherent summation over all receive element, delay-and-sum increases the image quality.

As can be seen in Figure 3.11, the beamforming calculations are based on the geometric model of the transducer elements and image point. Once the propagation path from a transmit element to a point

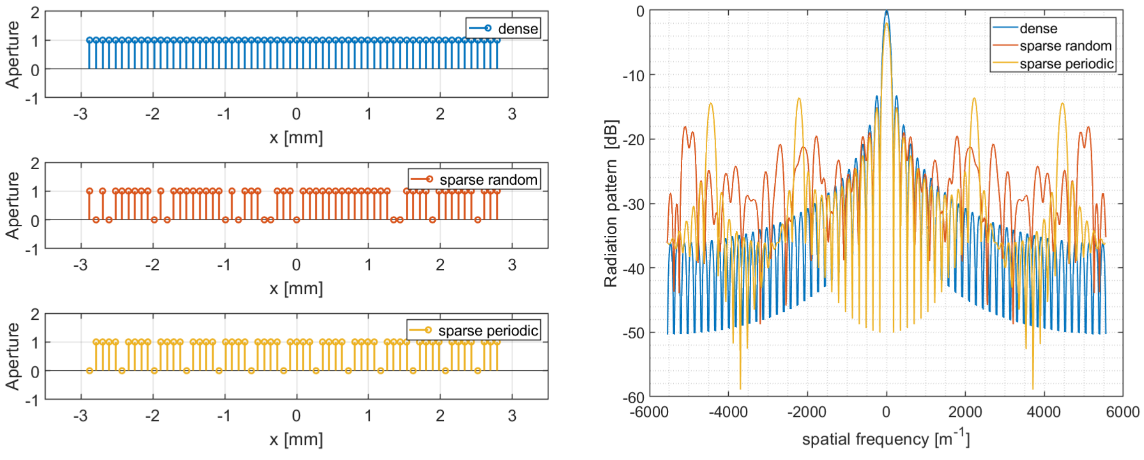

(a) (b)

Figure 3.10: (a) Three 64-element linear apertures showed as 1's in the figures. The removed elements for the sparse arrays are showed with 0's. (b) Radiation pattern for the three apertures. The horizontal axis represents the spatial frequency, which can be seen as the directivity towards different angles.

on the image plane and back to a receive element is known, the delay due to this propagation path can be calculated. In essence, every possible wavefront can be used for the transmission of ultrasound. What is important is to be able to model the wavefront of the transmitted wave. Simple wavefronts, such as spherical or planar wavefronts, make it simple to obtain a geometrical model. This means that synthetic aperture imaging, including PWI, can also use the regular DAS algorithm.

In general, the delay-and-sum calculation to obtain an image line for classic phased array imaging using static transmit focusing is

$$s(t) = \sum_{i=1}^{N_{RX}} a_i(t) g_i(t - \tau_i) \tag{3.4}$$

where $s(t)$ is an image line, N_{RX} the number of receive elements, $a_i(t)$ an optional apodization function, $g_i(t)$ the received element signal and τ_i the geometric delay from focal point to the RX element.

For synthetic apertures, the beamforming operation includes the summation of the individual transmit element and corresponding delays. The propagation path delay τ_i in (3.4) will not only be the time from focal point to receiver, but also the time from transmit element to focal point. This way transmit focusing can also be applied dynamically.

The propagation delay τ can in the synthetic aperture case be splitted into a transmit delay τ_{tx} and receive delay τ_{rx}. In (3.4) the summation $\tau_{i,j} = \tau_{tx} + \tau_{rx}$. In general

$$\tau_{rx}(i,j) = \frac{\left|\vec{r_p} - \vec{r_r}(i)\right|}{c_0} \tag{3.5}$$

and

$$\tau_{tx}(i,j) = \frac{\left|\vec{r_p} - \vec{r_t}(j)\right|}{c_0} \tag{3.6}$$

where $\vec{r_p}$ is the location of the focal point on the image plane, $\vec{r_r}(i)$ and $\vec{r_p}(j)$ the position of the receive element i and transmit element j, respectively. To obtain the time delay, the distances are divided by the sound velocity c_0 [52].

The beamforming equation for synthetic apertures has the same form as (3.4), but the summation has to be done over both the transmit and receive element.

$$s(t) = \sum_{i=1}^{N_{RX}} \sum_{j=1}^{N_{TX}} a_{i,j}(t) g_{i,j}(t - \tau_{i,j}) \tag{3.7}$$

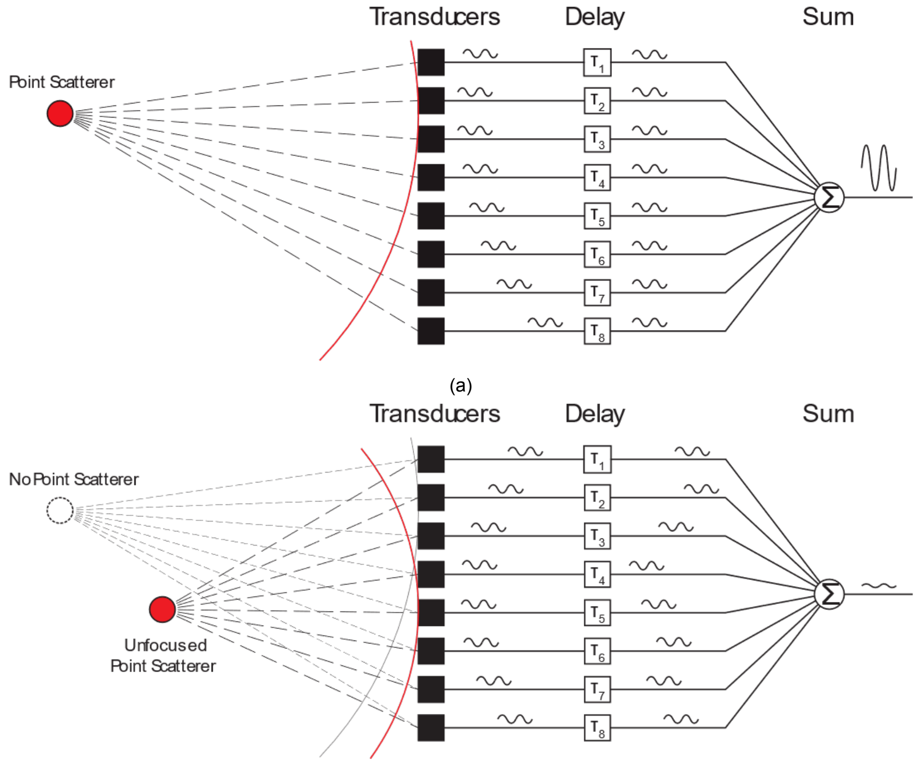

(a)

(b)

Figure 3.11: Delay-and-sum beamforming process. The delays $\tau_1 - \tau_8$ are generated to align echoes coming from the point scatterer in (a). Echoes from other scattering objects (b) arrive at different times at the array elements, leading to a incoherent summation and weak output signal.

where $s(t)$ is the beamformed signal for focal point $\vec{r_p}$, N_{TX}, N_{RX} the number of transmit and receive elements, respectively, $a_{i,j}(t)$ an optional apodization function, $g_{i,j}(t)$ the received signal at receive element i due to transmit element i and $\tau_{i,j}$ the geometric delay from transmit element to the receive element.

The implementation of DAS on hardware can be done in an analog or digital fashion. Switched capacitors can be used as an analog delay line for receive beamforming. However, large capacitances are needed to have long enough delays and to minimize the kT/C noise [38]. In [46], switched capacitor networks are used to pre-steer a sub-array of RX elements. This method of micro-beamforming does not require large capacitors, but the pixel still does not satisfy the $\lambda/2$-pitch. Other analog delay methods, such as switched-currents also require a large die area [53].

Digital beamforming is done by implementing the summations of (3.4) or (3.7) in software. After reception and amplification of the echo in the AFE, an ADC is added to digitize each individual element signal. While digital beamforming is more accurate, it increases the amount of on-pixel hardware [38].

3.5.1. Signal-to-Noise Ratio

Transmit and receive beamforming increases the image quality. For TX beamforming this is because higher transmit pressures lead to higher echo amplitude. Equally, RX beamforming coherently adds the backscattered echoes, also with an increase in amplitude as a result.

From previous work [11] it has been found that for FUS the focal pressure increases linearly with the number of transmit elements N_{TX}. A high focal pressure directly leads to echoes with a higher amplitude. The noise of a receiver N_0 remains equal, but the echo amplitude increases with the number of transmitter. If S_0 is the echo amplitude due to a single transmit element, the SNR at the receiver increases to $N_{TX}S_0/N_0 = N_{TX}SNR_0$. SNR_0 is the signal-to-noise ratio if a single element is used during transmit and receive.

If each RX element receives an echo with amplitude S_0, the coherent summation of N_{RX} elements leads to a signal with amplitude $N_{RX}S_0$. The noise N_0 is mainly due to the electronics. This is assumed

Table 3.1: conventional phased array (CPA) vs. classic synthetic aperture (CSA)

	CPA	CSA
TX focusing	Static	Dynamic
RX focusing	Dynamic	Dynamic
Frame rate	Low	High

to be uncorrelated thermal noise. Therefore, the noise amplitude after summation is $\sqrt{N_{RX}}N_0$. The SNR of the overall pulse-echo scan will then be $N_{RX}S_0/\sqrt{N_{RX}}N_0 = \sqrt{N_{RX}}(S_0/N_0) = \sqrt{N_{RX}}SNR_0$.

In general, the SNR at a point reconstructed from pulse-echo sequences with beamforming in transmit and receive can be given by [51]

$$SNR\ (\text{dB}) = 20\log_{10}(N_{TX}\sqrt{N_{RX}}) + SNR_0. \tag{3.8}$$

From this, it can be seen that beamforming with many elements significantly increases the image quality. Besides, the influence of the number of transmit elements is greater than having a large number of receiver element. This, however, does only hold for transmit focusing in the case of classic phased arrays. It was found that for plane waves the local pressure does not increase beyond a certain array size.

3.5.2. Frame Rate

Besides the SNR, the time required to obtain an image is also an important factor for comparison. It seems that synthetic aperture imaging needs more pulse-echo sequences than conventional phased array (CPA) imaging. This is because in the conventional case the entire aperture is used at once, while N sequences are needed in Figure 3.5. The difference is that once the complete aperture has been synthesized, beamforming can be applied to entire data set. Since CPAs use static transmit beamforming, the focus spot has to be moved through the image plane. For synthetic aperture imaging, there is no direct focusing during transmission. However, after all pulse-echo sequences are obtained, the transmit focus can dynamically be move by applying adding different transmit delays to the beamformer. The comparison between CPA and CSA can be seen in Table 3.1.

However, CPA uses static transmit beamforming, where the image is acquired by sequentially scanning one image line at a time. The number of pulse-echo sequences is therefore the scanning sector size divided by the sampling interval. In order to create a 2D image of a 90° sector with 0.5° sampling intervals, 180 pulse-echo sequences are required. Depending on the receive architecture, this can be a multiple of this number. For a 3D image, the entire imaging volume has to be scanned, which dramatically increases the number of sequences. If in the previous example also a 90° sector in the other plane has to be images, a total of $180 \times 180 = 32400$ sequences are needed [42].

For classic synthetic aperture imaging, the number of transmit-receive sequences is the number of elements in the array. This means that to obtain a volume scan for 3D imaging, $64 \times 64 = 4096$ pulse-echo sequences are needed. The advantage of synthetic aperture imaging is that once the volume is scanned, transmit and receive beamforming can be done by post-processing the data set and changing individual delays.

4

System Design

In the previous Chapter 3, the many possibilities of using 2D-arrays for focused ultrasound and imaging were stated. These will serve as a design space for this chapter. First, the specifications and requirements for the proposed system are be obtained. Next, the requirements in combination with the design space will converge towards a system design for the integration of FUS neuromodulation and imaging.

4.1. System Requirements

As mentioned in the previous chapter, the system should be capable of both CW and PW transmission. For both functions precise phase differences between adjacent elements need to be generated. The phase difference depends on the location of the focal spot. A larger focal depth results in less phase differences between channels, while large differences are needed to focus near the array. This can be seen by making an analogy to optical lenses: a bigger (more convex) lens has a smaller focal length then a smaller lens.

In mice, the vagus nerve depth is around 4 mm [54] with a nerve diameter of 200 μm [55]. Together with the CCA and IJV they form a recognizable area on the image (recall Figure 1.1). In order to obtain a good field of view, the focal depth N is set to be variable from $1-5$ mm. The focal area can be characterized by spatial lateral resolution S_{lat} (full width at half maximum), spatial axial resolution S_{ax} (depth of field of the focal area), near-field depth[1] Z_{max} and focal gain $G = p_f/p_0$ (determined by the ratio of peak pressure at the focal spot p_f to the pressure at the transducer interface p_0. The properties are related to the wavelength λ, lateral dimension of the square aperture L and focal depth Z_m and can be stated as

$$S_{lat} \propto \frac{\lambda Z_m}{L}, \tag{4.1}$$

$$S_{ax} \propto \frac{\lambda Z_m^2}{L^2}, \tag{4.2}$$

$$Z_{max} \approx \frac{L^2}{\pi\lambda}, \tag{4.3}$$

$$G = \frac{p_f}{p_0} \propto \frac{L}{\lambda Z_{max}}. \tag{4.4}$$

From these relations it can be found that to have a high-resolution, high-intensity focal area the array should be large in size and the frequency should be high. Since the $\lambda/2$-pitch requirement determines the size of the array element, creating a large aperture significantly the number of element. This makes it very difficult to implement a fully sampled array.

To effectively modulate the nerve, a lateral resolution of $S_{lat} < 200$ μm is needed. This, together with the previous obtained parameters, yields a lateral aperture dimension of $L = 3.2$ mm. The required

---

[1] For rectangular arrays better numerical approximations can be found [56].

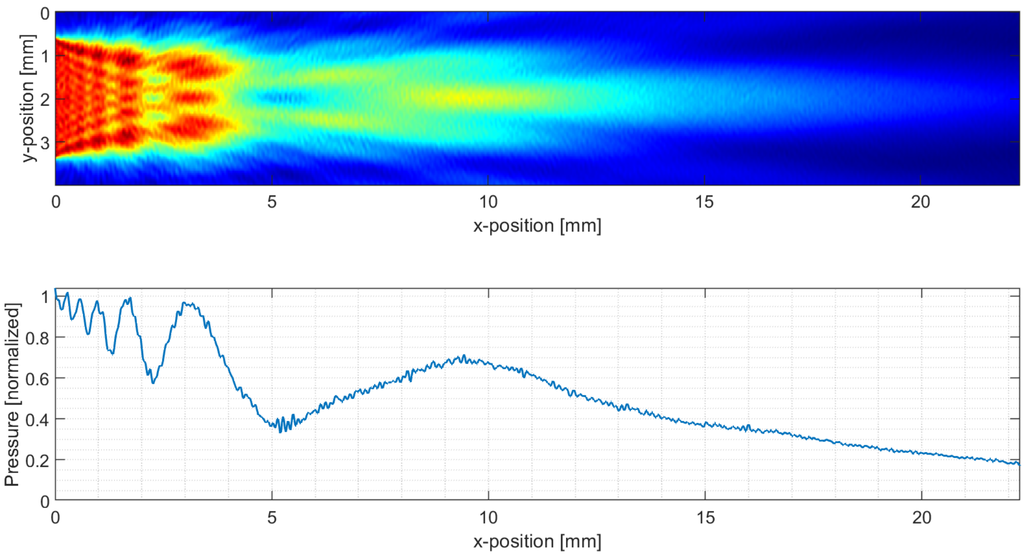

Figure 4.1: Ultrasound beam pattern for a 32×32 element array. The array is positioned at the left size of the image and the root mean square (RMS) pressure at every location in the image plane is plotted. Red colors correspond to a high pressure. At distances close to the array, the local pressure distribution changes quickly. After a last peak at $x = 9.5$ mm, the pressure gradually decays. At this point the far-field region is entered. The bottom figure shows the axial pressure through the mid-line of the array ($y = 2$ mm).

F_r	8.4 MHz
λ	180 µm
Z_m	4 mm
Z_{max}	7 mm
S_{lat}	200 µm
Array size	64×64

Table 4.1: Used system parameters.

focal depth should be amply exceeded by the near-field depth Z_{max}, after which the focal spot intensity and resolution quickly decreases.

In Figure 4.1 a simulation for the beam profile of a 32×32 array can be seen. The medium is composed of soft tissue. No relative phasing is applied to the array, so the beam profile shows the natural focusing behaviour of the aperture. In the top figure, the root mean square (RMS) pressure for every location in a plane through the middle of the array can be seen. Around 10 mm depth a last high-intensity area can be seen. This corresponds to the natural focus depth of the aperture. The near-field depth is the depth at which this last local peak occurs. The approximation of (4.3) gives an near-field depth of 13 mm.

For high-quality imaging, the axial resolution $S_{ax} \propto BW = F_r/Q$, where BW is the bandwidth of the pulse wave, F_r the resonance frequency and Q the quality factor of the transducer. This means a short pulse (1 period) should be emitted with a wide bandwidth transducer.

Continuing on previous work [11], [12], the chosen array specifications can be seen in Figure 4.1. Since this thesis describes the a concept for system-level design, the exact parameters can be modified.

The proposed system should be able to apply both focused ultrasound neuromodulation and imaging of the target area. The combination of imaging and neuromodulation means that the system should have three main functions:

F1 Transmission of high-intensity focused CW for neuromodulation.
For neuromodulation long pulse durations are needed to reach the required energy to achieve

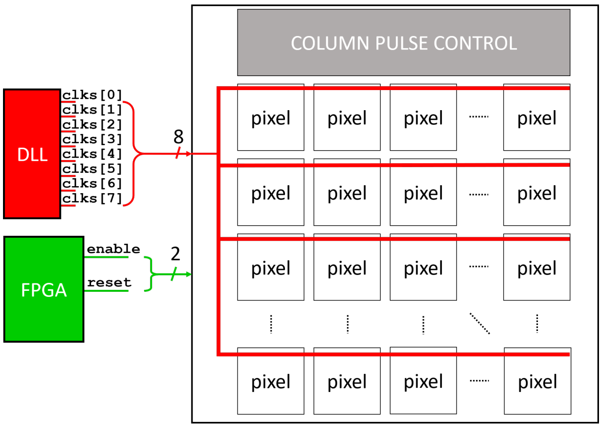

Figure 4.2: Array design when continuous wave mode (neuromodulation) is active. The delay-locked loop (DLL) phases will be directly distributed to the pixels. Inside the pixel the correct phase is selected using the `phase_select` register seen in Figure 4.5 .

stimulation. Depending on the amount of transmitted power, pulse durations can be in the order of several hundreds of milliseconds [23]. At 8.4 MHz, this relates to thousands of high-frequency cycles continuously. The long duration simplifies the phase control of the transmit beamformer. While the required phase differences for focusing can span multiple periods, the continuous wave nature allows for wrapping the phases back to the interval $[0, 2\pi)$. The resolution of the focal spot is determined by the physical properties of the imaging system (array dimensions, focal depth and wavelength).

F2 Transmission of PW for imaging.
Pulse-echo imaging requires short pulses to obtain echo signals with high spatial resolution [28]. Between the transmission of subsequent pulses should be enough time for the echoes of the deepest point of interest to be received.

F3 Receiving the echo signals for imaging.
In prior work a single receive channel is designed [12]. However, the silicon area of a single RX channel exceeds the $\lambda/2$ pitch requirement. Improvements have to be made in order to make a channel fit in the required area. Because the depth of field is quite shallow (only $\sim$ 5 mm), the attenuation versus time is low. The time-gain compensation (TGC) could therefore be simplified or even removed. Another possibility is adding programmable gain to the low-noise amplifier (LNA) [57], which could make the TGC redundant.

4.2. Architecture Design

The system requirements specified at the beginning of this chapter make it impossible to implement a fully sampled 2D-array where each pixel has both TX and RX capabilities. Jensen and Nikolov [45] state that “[i]deally, we would like to create a large imaging aperture without an increase in the number of processing channels.” The many possibilities of using 2D-arrays for focused ultrasound and imaging stated in Chapter 3 will serve as a design space. This section will use this design space, together with the earlier mentioned requirements, to design the architecture of an array that can be used for both FUS neuromodulation and imaging.

For neuromodulation mode the DLL outputs should directly be connected to the individual pixel. Since neuromodulation is done using focused ultrasound, the phase can be different for each element. This means that the selection of one out of the eight phases can only be done on-pixel. The eight DLL clocks `clks[7:0]` are directly fed into the pixel for neuromodulation. Refer to [11] for a detailed analysis on the design of a DLL.

4.2.1. Neuromodulation Mode

The generation of a high-intensity focal area with the spatial resolution the nerve diameter is done by focusing ultrasound with a phased array. Long pulse durations are needed to transmit enough energy

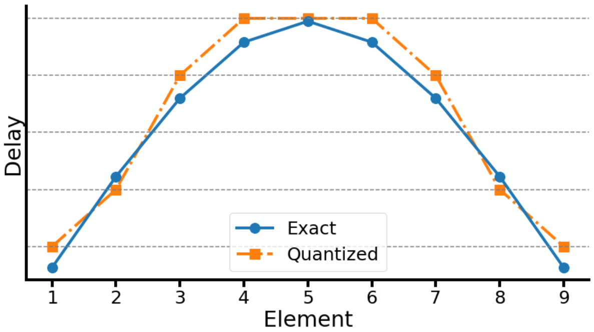

Figure 4.3: Ideal (blue) and quantized (orange) delay profile for a nine-element array. The quantization levels are shown as the grey dotted lines.

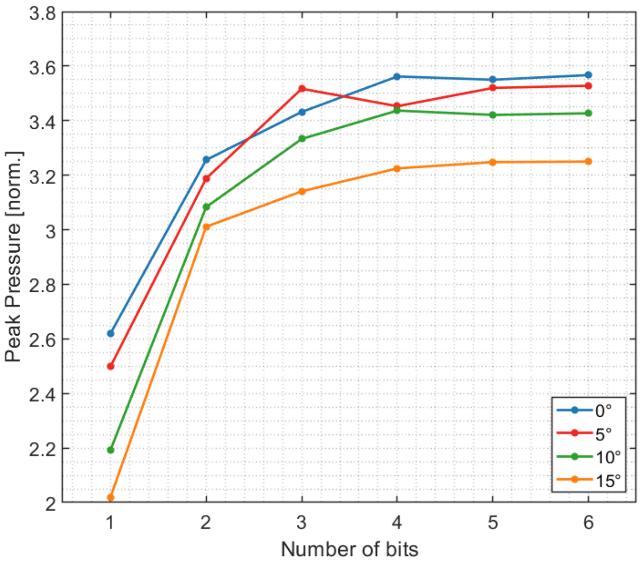

Figure 4.4: Peak pressure of focal area for varying levels of delay quantization (number of bits) and steering angles.

for the elicitation of action potentials in the axon. Generating the required phases for the phased array is done using a delay-locked loop. The DLL outputs multiple clock signals with different delays. The delays are discrete in nature, hence a design decision has to be made on the quantization level of the delays. The quantization error leads to the spreading of the focal area, reducing its peak pressure. Figure 4.3 shows the quantization of the delays. Previous work [11] uses a 3-bit DLL combined with an on-pixel phase interpolator to gain an additional 3-bits in the phase profile. Delays with a least-significant bit delay of $T_{LSB} = T_0/2^6$ are obtained, which leads to focusing with a high focal pressure. More recently [58], it was found that reducing the number of bits is possible without losing significant focal pressure. A reduction in the phase can lead to a complete elimination of the on-pixel phase interpolation, which is beneficial for the small pixel size in this work.

To verify the reduction in quantization levels, a focused ultrasound MATLAB simulation is done. Figure 4.4 shows the peak pressure at the focal spot varying the number of quantization bits and steering angles. While the pressure for $n_{bits} \geq 4$ reaches a high plateau, a 3-bit DLL seems a good trade-off between reaching sufficient focal pressures while maintaining a simple implementation. Since the DLL is shared across all TX element, the clock phases have to be routed to every element. Hence, every additional bit doubles the amount of wires, making it increasingly difficult to implement.

For a clock period of 120 ns, the delay quantization T_{LSB} = 15 ns. In the figure, the complete [0, 2π) phase map is generated. It would be possible to generate only half of the phases (from [0, pi)) and use an on-pixel clock inverter to add an additional 180° to the phases. This halves the number of wires coming out of the DLL. For the rest of this thesis, the DLL is assumed to generate all eight phases.

4.2.2. Imaging Mode - Transmission

Creating clock signals with specific phases is different from creating single pulses with specific delays (see Section 2.4). Common imaging systems employ an on-pixel transmit beamforming architecture. Each pixel has a register which holds the required delay information. An off-pixel counter value is compared with the delay register and when the counter equals the register value, a one-shot pulse is triggered. This (low-voltage) pulse feeds into a level-shifter and high-voltage transducer driver [59].

For linear arrays, there is often enough silicon area to incorporate such counter-based architectures within the pixel. In the case of a high-frequency 2D-array, as in this project, the element size does not allow the implementation of the such architectures. The combination of needing both continuous waves for neuromodulation and pulsed waves for imaging makes this even more difficult.

Using a synthetic transmit aperture can eliminate the need for precise timing generation. In the classic synthetic aperture scheme of Section 3.2 only one TX element is active at a time. Hence, no delay generation is needed. A common one-shot pulse generator could be connected to each consecutive TX element, simplifying the on-pixel hardware. Transmit beamforming can dynamically be done in hindsight when the entire array is synthesized, but the lack of transmit pressure still limits the SNR [42], [45].

Multiple element have to be used at the same time to increase the transmit pressure, but no complicated delay generation for the pulses should be necessary. A synthetic aperture imaging technique that fits these requirements is PWI, mentioned in Section 3.3. It was concluded that PWI can be a useful technique for the reduction of hardware, minimization of imaging time (allowing high frame rates) and still be able to apply dynamic transmit beamforming to increase the image quality throughout the entire image plane. Since a plane wave is transmitted, the delays between two adjacent elements is the same across the entire array. Since the near-field depth of a 64-element wide array with 90 µm pitch is over 5 cm, the natural focusing of the aperture does not influence the plane wave transmissions.

In Chapter 3.5 it was concluded that any synthetic aperture imaging technique can use DAS beamforming as long as the wavefront can be accurately modelled. Since PWI uses plane waves (obviously), the wavefront is easy to model. Nikolov [45] obtains the geometrical model for angled plane waves as can be seen in Figure 4.6. A virtual rotation point, τ_v seconds behind the transducer, is used as the source of the plane waves. The propagation delays can then be expressed as

$$\tau = \tau_v + \frac{z\cos\alpha + x\sin\alpha}{c_0}. \tag{4.5}$$

Usually, the plane wave angle is specified and the appropriate inter-element delay is calculated [44]. While the inter-element delays are equal, it still requires precise phase control for the pulse generation. In this thesis, a novel pulse generation method is implemented. The working principle is based on using the already available phase information generated by the shared delay-locked loop instead of having a dedicated phase generator for pulsed wave mode. Instead of specifying the plane wave angle and calculating the delays, the inter-element delays are specified and the angle is calculated afterwards.

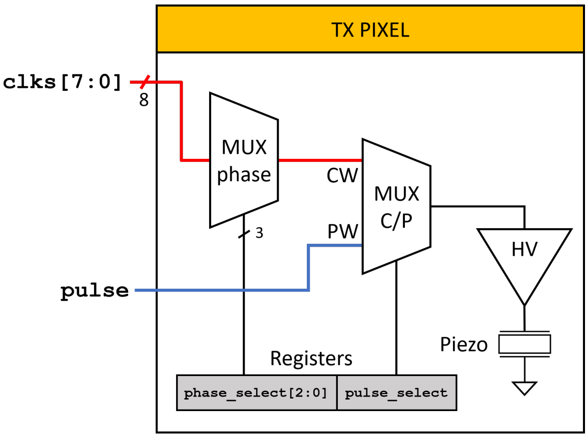

Figure 4.5: System architecture of the transmit pixel.

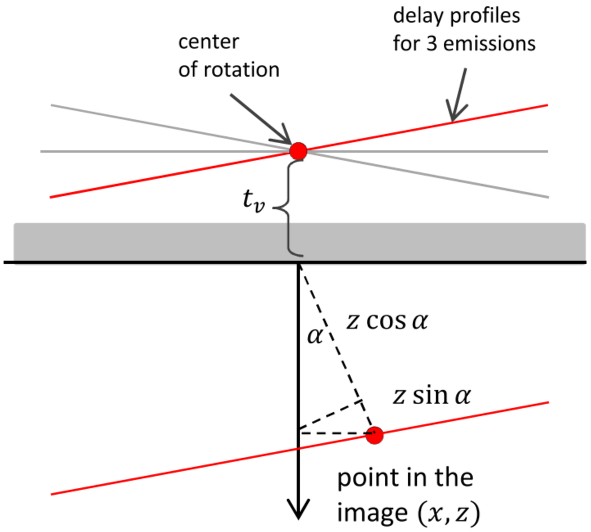

Figure 4.6: Geometric model for angled plane waves. By providing a virtual rotation point behind the transducer.

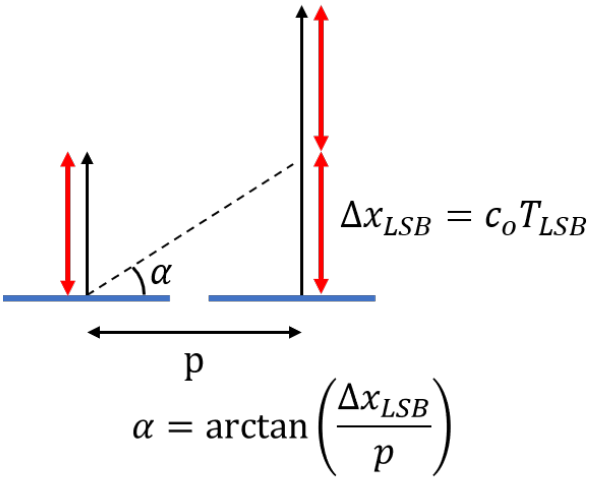

Figure 4.7: An array with pitch p and inter-element delay T_{LSB} defines the steering angle α for the plane waves.

The DLL generates 3-bit phases of a 8.4 MHz input clock. This means the least-significant bit corresponds with a delay of

$$T_{LSB} = \frac{1}{2^3 \cdot 8.4\,\text{MHz}} = 15\,\text{ns} \tag{4.6}$$

If this T_{LSB} can somehow be extracted from the continuous phases, it can be used to trigger a single pulse with the correct delay. For a plane wave, the delay between two adjacent elements is equal throughout the array. By having the delays be an integer multiple m of T_{LSB}, the angle changes. It is also possible to combine multiple columns n with the same array. This effectively increases the pitch to $n \cdot p$. For an array pitch $p = 90\,\mu\text{m}$ and delay of $T_{delay} = mT_{LSB}, \quad m = 1, 2, 3, 4$, the corresponding angle will be

$$\alpha_n = \arctan\left(\frac{m \cdot c_0 T_{LSB}}{n \cdot p}\right). \tag{4.7}$$

Figure 4.7 clearly illustrates the definition of the angle for multiple T_{LSB} delays between the element. The resulting wave profile for various number of columns per T_{LSB} can be seen in Figure 4.8. To get a better idea of beam profile, the plane wave are transmitted continuously instead of only transmitting a single pulse. It can be seen that the plane wave angle changes when the number of columns with equal

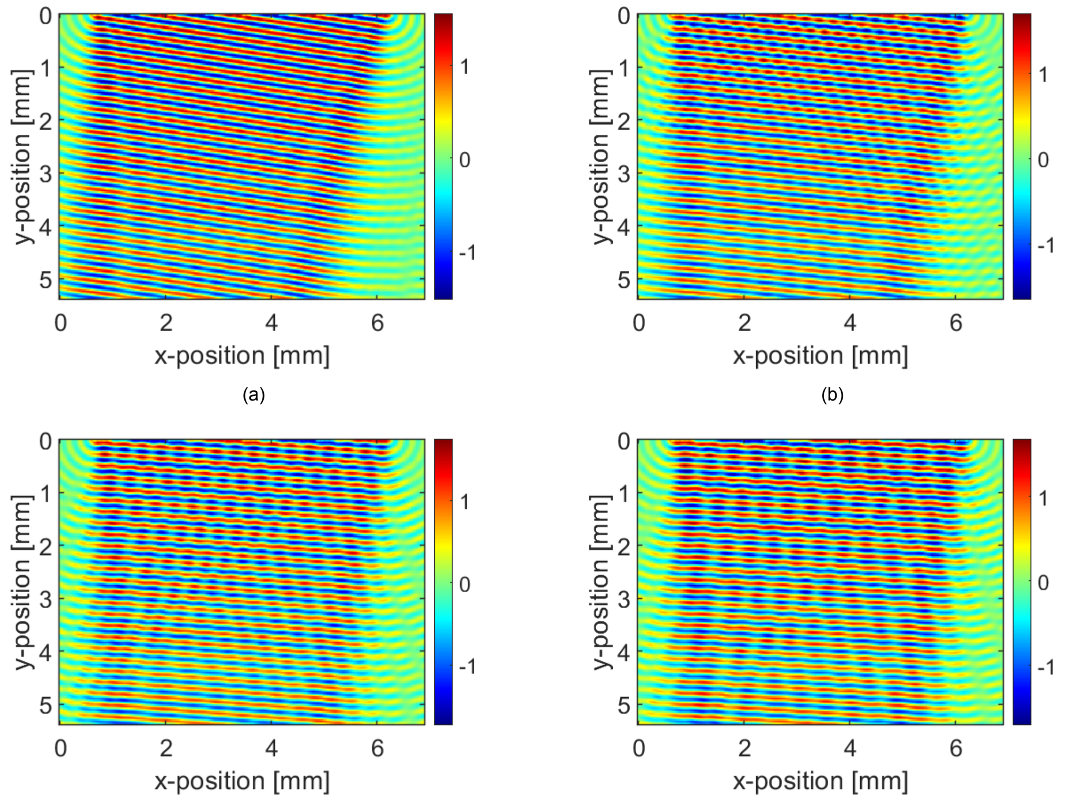

(a) (b) (c) (d)

Figure 4.8: Plane-wave transmission for different number of columns (n in (4.7)), $m = 1$) per T_{LSB}: (a) $n = 2$ giving a 7.3° steering angle, (b) $n = 3$ giving a 4.9° steering angle, (c) $n = 3$ giving a 3.6° steering angle and (d) $n = 5$ giving a 2.9° steering angle.

phase increases. Due to the phase quantization of the DLL and implementation of the plane waves, a slight staircase pattern can be seen in the waves when a next column changes to a different phase.

With increasing m the angle quickly increases. For $m = 1$, the angle is 14.4°, while for $m = 2$ this is already 27.1°. Increasing n asymptotically reduces the angle, with a 0° angle if all columns as connected to the same phase ($n = 64$). Table 4.2 shows the angles for higher m and n. In practice, $m \geq 2$ will lead to angles that steer the beam away from the imaging volume.

Figure 4.9 shows the gate-level implementation of the pulse generator. The pulse generator can be seen as a logic block that extracts a single period (a pulse) from an input clock. The generator is build around a D flip-flop (DFF) counter element. The DLL (not shown) outputs eight phases `clks[7:0]` of an input clock. The phases are separated by 45°. Two quadrature phases (90° phase difference) out of the eight phases will be fed into a XOR-gate. If the clocks of the DLL are at frequency F, the XOR-output will be a clock signal with frequency $2F$. The frequency doubling is necessary since the DFF acts as a clock divider because the inverted output $\overline{Q_{DFF}}$ is fed back to the input (through the AND-gate). Thus, XOR_1 and XOR_2 are clock signals with frequency $2F$. The output XOR_2 is the clock input of the DFF. At the rising-edge of XOR_2 input, the state of the D-input will be transferred to the output signals Q_{DFF} and $\overline{Q_{DFF}}$. The AND-gate combines multiple signals to make sure the DFF D-input is only high when it needs to be. The D-input is only high when:

1. No pulse has already been generated by the channel. When `pulse` is high, it triggers the SR-latch such that $\overline{Q_{SR}}$ is low. This forces the AND-gate to a low output.

2. Enable is high. This is an external input that signals when the system should enable imaging mode instead of FUS for neuromodulation.

3. XOR_1 is high. Since this signal leads XOR_2 by 90°, it makes sure that a `pulse` will only be generated at the first rising-edge of XOR_2. This preserves the delay information of the DLL.

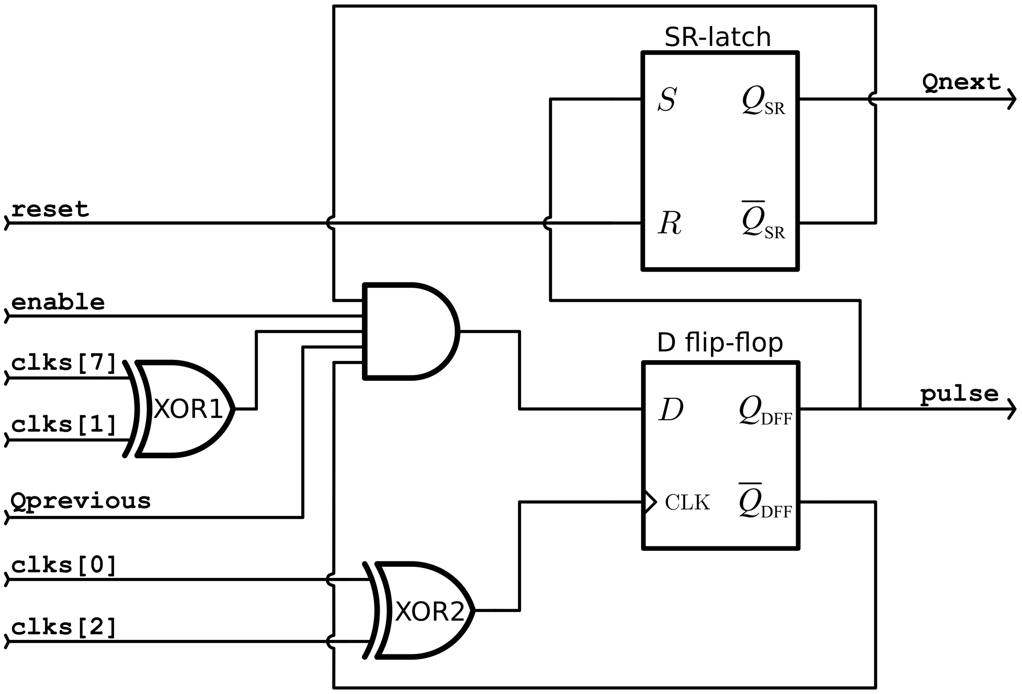

Figure 4.9: One-shot pulse generator from continuous DLL phases.

Table 4.2: Plane wave angle for different delays. By varying parameters m and n a multiple of the least-significant delay T_{LSB} or a combination of multiple transmit columns with the same phase is chosen, respectively.

m	n	angle
1	1	14.4°
1	2	7.3°
1	3	4.9°
1	4	3.6°
2	1	27.2°
2	3	9.7°
3	1	37.6°

4. `Q_previous` is high. For this plane wave imaging implementation the output pulse is generated after the previous pulse has been generated. The `Q_previous` input of one column is connected to the `Q_next` output signal of the previous channel.

5. the `pulse` output is high within one time period. The feedback of $\overline{Q_{DFF}}$ back to the input makes sure `pulse` is only high for $1/2F_{res}$.

A summary of the input and output signals of the pulse generator can be found in Table 4.3.

To test the functionality of the pulse generator from Figure 4.9, the system has been designed using structural Verilog and a simulation has been performed. The signal waveforms can be seen in Figure A.1. A master clock `mclk` with period $T = 120$ ns is fed into a DLL. The output phases are present as the eight clock signals `clks[7:0]`. It can be seen that the phases are separated by 15 ns, which equals the 3-bit phase quantization (120 ns/2^3).

For this simulation eight consecutive output pulses are generated. These can be seen as signals `pulse[7:0]`. The pulses have the same phase information as the clocks from the DLL, but with only a single period. To test the reset functionality, a `reset` signal has been created with a rising-edge around 200 ns. It can be seen that as soon as the reset signal triggers, the output phases immediately go to a low level. After `reset` is low, the pulse generation will start at the next clock cycle.

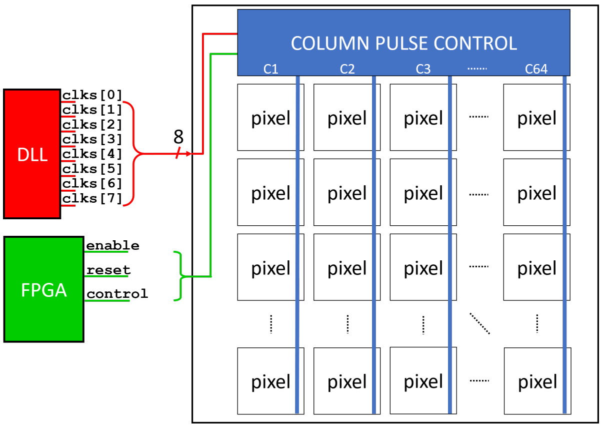

Figure 4.10: Array design for plane wave imaging (PWI) implementation. The delay-locked loop (DLL) phases will be connected to the Column Pulse Control block, where the pulse of each column is generated using the pulse generator from Figure 4.9.

The pulsed wave `pulse[0]` is the first pulse that is triggered from the clock phases. Since the pulse generators have the `Q_previous` input, the subsequent pulses are only triggered when the previous pulse has been triggered. It can be seen that after a single pulsed wave, no other pulses are triggered despite the continuing clock phases.

Because the plane wave angle can be adjusted, the columns must be able to select multiple phases. In order to do so, a multiplexer inside the CPC selects a phase out of the generated pulses. In Figure 4.10 the architecture during pulsed wave transmission can be seen. All elements in a column are connected together so that the 2D array reduces to a wide linear array. It might be possible to also implement the same pulse control for rows, so that plane wave with angles in two dimensions can be sent out. This could be useful for 3D imaging, but it is beyond the scope of this application.

Figure 4.5 shows the implementation of a transmit pixel. Only two multiplexers, a register to hold configuration data and the transducer driver is present inside the pixel area. The piezoelectric transducers, described in Section 2.3, have to be excited with a high voltage to generate enough acoustic pressure at the surface. Despite the fact that piezoelectric transducers like PZT and do not require the high biasing voltages needed for CMUTs, the excitation voltages are still higher than typical CMOS compatible levels. Switching high voltages requires transistors that can handle the electric fields. Usually double-diffused metal-oxide-semiconductor (DMOS) transistors are used. These transistors usually occupy a large area, which makes it difficult to design a pixel-matched HV driver for small pitch 2D arrays. Alternatively, stacked LV CMOS compatible transistors can be used for the driver circuit. The stacked topology splits the required high supply voltage across multiple drain-source voltages [60]. The use of standard transistors eliminates the need for a HV process and reduces the area occupied by the large DMOS transistors. In [11], the design of the transmit pixel is described.

Signal	Description
`reset`	Active-high external input signal that forces PULSE low.
`enable`	Active-high external input signal that triggers the generation of a pulse.
`clks[]`	One of the eight output phases from the shared DLL.
`Q_previous`	Q-output of the SR-latch from the pulse generation block from the adjacent column.
`Q_next`	Q-output of the SR-latch from the own pulse generation block indicating the pulse of the next block can be generated.
`pulse`	Output signal with a single high pulse generated from the continuous delay-locked loop (DLL) phases.

Table 4.3: Description of the signals from Figure 4.9.

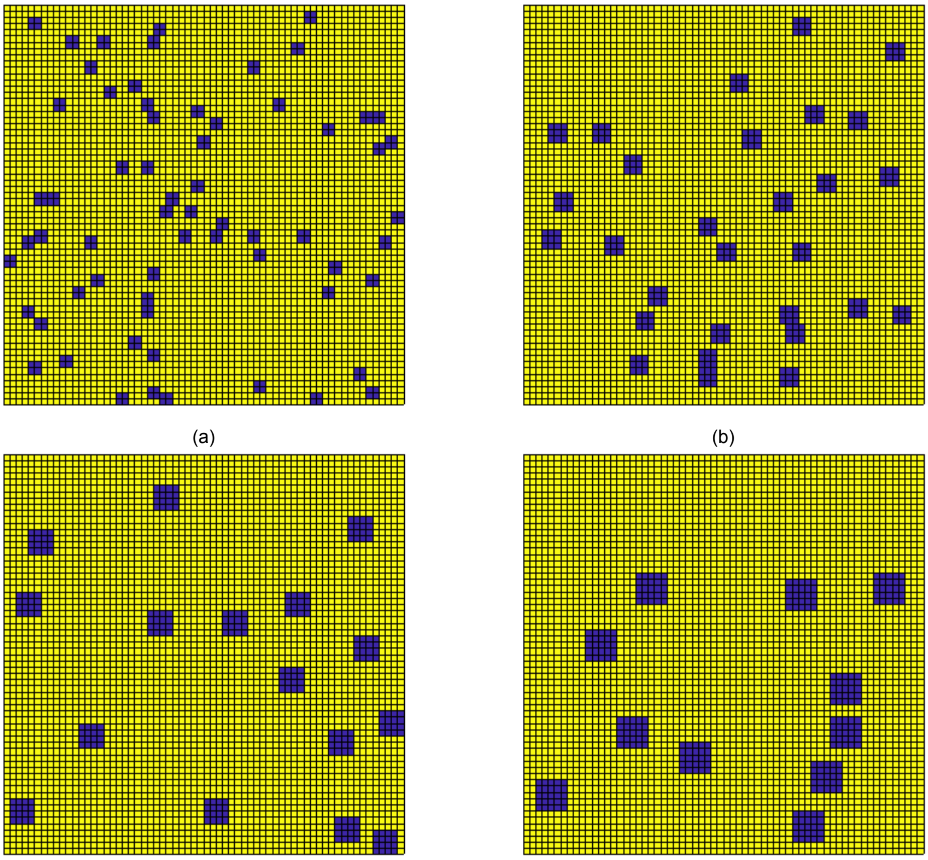

(a) (b)

(c) (d)

Figure 4.11: A 64×64 array (yellow) with sparse randomly populated sub-arrays (purple). The sub-arrays are (a) 2×2 elements, (b) 3×3 elements, (c) 4×4 elements and (d) 5×5 elements. In each case the total number of removed elements will approximately be the same.

4.2.3. Imaging Mode - Reception

For the receive channels the same design philosophy as in the previous sections holds. An architecture has to be found to implement the receive channels for ultrasound imaging using the less amount of on-pixel. Since the transmit elements cannot be equipped with receiver channels, dedicated receive elements have to be included on the array. These elements do not contribute to the focal pressure for FUS neuromodulation, so only a minimal amount of RX elements should be present. As in Section 4.2.2, the classic synthetic aperture imaging scheme can be used as the basis for the receive architecture. The receive signal chain can be split into the AFE and the beamformer. The AFE provides signal conditioning and amplification to the (weak) signal coming from the piezo elements. Beamforming can take place before or after digitization of the (analog) signal. Digitization is needed for further digital signal processing and creation of the image. Since the envisioned goal is to apply image recognition, the image needs to be transformed to the digital domain at some point in the signal chain.

One possibility is to use small sub-array of RX elements surrounding the TX elements. However, the receive aperture will then be small. Since it is possible that the location of the vagus nerve is in a far corner of the focusing volume, the directivity should be good for every angle. The implementation of random sparsity leads to a minimal loss in overall directivity since the apertures do not change much. No additional side lobes due to the periodicity of the sparse elements will be generated [61].

Previous work has already shown that the focal pressure linearly decreases with an increase in sparsity (i.e. the number of removed elements in the array) [11]. This is because for a phased array every element contributes approximately equal to the pressure at the focal spot. However, it is still unclear if the grouping of the sparse elements has an influence on the focal pressure and beam profile. A MATLAB simulation has been performed to explore the influence of the sparse sub-arrays on the focal pressure and beam profile. An array of 4096 (64×64) elements is created and random sparse

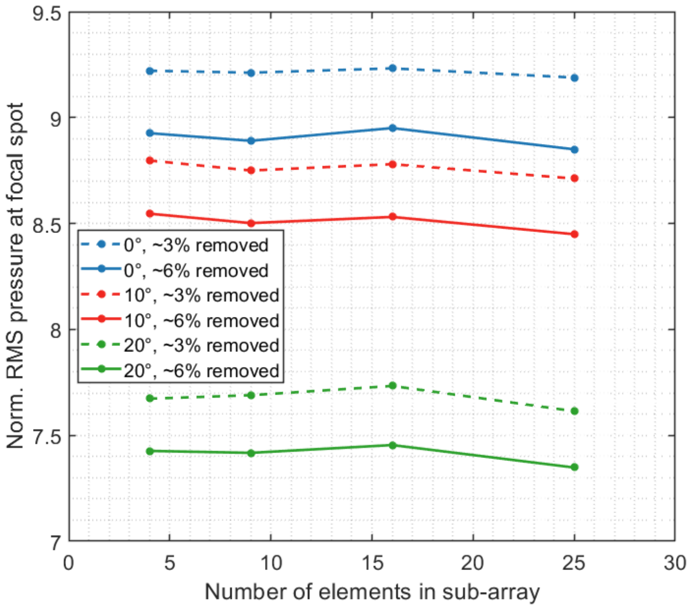

Figure 4.12: Normalized root mean square (RMS) pressures at the focal spot for various steering angles and number of removed elements. The solid lines are when ∼6% of the elements in the array are removed. The dotted lines when ∼3% is removed.

sub-arrays are placed across the array. The sub-array size is varied from 2×2 to 5×5 elements. To be able to compare the results, the total number of removed elements is held constant. The goal was to remove 128 and 256 elements from the 4096-element array. This comes down to removing 3% and 6% of the total elements, respectively. Since the number of removed elements is an integer multiple of the sub-array size, the exact number varies. In Table 4.4 the number of sparse elements for different sub-array sizes are shown.

Figure 4.12 shows the normalized pressure at the focal spot with respect to the pressure at the surface of the array. Different steering angles and number of removed elements are simulated and plotted. It can be seen that the focal pressure remains constant for all sub-array sizes. Only the pressure of the 5×5 sub-array is slightly lower, but this is due to a larger number of removed elements (Table 4.4). In Figure 4.13 the beam profiles of the various sparse arrays at a steering angle of 0° and 20° can be seen. The dimension of the focal spot remains equal for all sub-arrays. For large sub-arrays the pressure outside of the focal region is less uniform with higher (unwanted) peaks than the beam profile for small sub-arrays. However, the variations are small. It can be concluded that the intensity and dimension of the focal area is independent of the sub-array size. Only the degree of sparsity plays a role in the focal intensity, which is expected since less elements contribute to the pressure at the focus spot.

The application of large sub-arrays can be useful for the implementation of the receiver channels. By implementing a single receiver channel on a sub-array, more silicon area is available since it is no longer bounded to a single pixel. A trade-off arises between the size of the sub-arrays (i.e. simplicity in implementation) and the imaging frame rate.

The implementation of synthetic aperture imaging reduces hardware complexity on-pixel, but it will shift more workload towards the digital processing unit. The envisioned wearable device is capable of applying image-recognition algorithms to extract the location of the vagus nerve from the cross section of the neck. This algorithm will be run on an field-programmable gate array (FPGA). The delay-and-sum algorithm should efficiently be implemented. Variations and optimizations of the classic DAS algorithm have been proposed for implementation on FPGAs [62], [63]. Since the delay calculation consists of continuously the propagation path, many multiplications and square root operations are needed.

A typical receive front-end consists of an low-noise amplifier stage and time-gain compensation amplifier [38]. The incoming echo signal is transformer into an electrical signal by the transducer elements. Then, the signal is conditioned by the analog front-end. The AFE provides a proper input impedance for the piezoelectric elements and amplifies the weak signal. As mentioned in Section 2.2, the TGC is needed to account for the increasing attenuation of the echo for larger imaging depth. By keeping the amplitude at a fixed amplitude, the analog-to-digital converter can use its full resolution to digitize the data. Since the depth of interest is very shallow, the use of time-gain compensation in this design is omitted.

The results from Section 3.4 prove useful for the implementation of the ultrasound receiver. During neuromodulation, as many elements should be used for the transmission of focused ultrasound. The use of sparse receive arrays minimizes the amount of pixels without transmit capabilities. Sparse receive elements can be placed at random locations across the array, minimizing the grating lobes for all steering angles in both azimuth and elevation direction.

The synthetic aperture imaging scheme allows the decoupling of the number of transmit elements from the number of receiver channels. Together with the independence of the the sparse sub-array size, this can be a useful architecture for the receive channels. Therefore, a synthetic receive beamforming using sparse sub-arrays scheme is created. Since multiple RX element can be combined into a sub-array, a single receiver can be implemented with an effective area of $A_{RX} = N_{RX,sub}A_{pixel}$. There exists a trade-off between the receiver sub-array size and the time needed for imaging. If in total 256 RX elements are present on the array, the sub-array size versus the number of pulse-echo sequences can be seen in Table 4.5.

An increase in sub-array size reduces the number of receivers, but a longer imaging time will be needed since the multiplexing of many element to the receiver increases. Not only needs the imaging time have to be minimized to have the longest available time span for neuromodulation, also synthetic aperture imaging suffers from increased motion artefact.

For an imaging depth of $Z_{max} = 7$ mm the round-trip time $T_{RT} = 9$ µs. For a sub-array size of 16 elements, the time to synthesize a full receive aperture is 150 µs. This is multiplied by the number of plane waves that have to be transmitted. For a number of angles $n = 9$ the total time to acquire an image frame is below 1.3 ms. The short time allows long pulse durations for neuromodulation while still being able to have multiple frames/s frame rates. Sub-microsecond motion artefacts are unlikely to happen at the location of interest. Breathing, heart rate pulses in the carotid arteries and movement of the neck will be the most common moving elements. It is not expected that these factors require high frame-rates before sharp images are obtained.

For a pixel pitch of $p = 90$ µm, the implementation of a 4×4 sub-array increases the available area for the receiver channel to 360×360µm^2. This is a four-fold increase in silicon area from the channel designed in [12]. Only an additional 16-to-1 multiplexer at the input of the front-end is needed to select each consecutive RX element. The 4×4 sub-array corresponds to Figure 4.11(c).

4.3. Final Design

In this section a summary of the system design will be given. The designed ultrasound VNS consists of 2D-array of 64×64 pixels that can be reconfigured into different modes. For neuromodulation, the array works as a classic phased array. A 3-bit DLL generates eight phases to obtain a high-resolution, high-intensity focal area with a minimum number of on-pixel TX hardware.

Imaging is done by combining plane wave transmission using inter-element delay controlled angles with a sparse synthetic sub-array receive aperture. Plane wave imaging eliminates the need for pulse phase control since existing phase differences are used for the generation of pulsed waves. Sparse sub-arrays minimize the loss in focal pressure for FUS and increases the available area for a sub-array shared receiver chain.

The array design can be seen in Figure 4.14. The pixel implementation was discussed in previous

Table 4.4: Exact number of removed elements for different sub-array sizes and percentage of removed elements.

Size	3%	6%
2×2	128	256
3×3	135	261
4×4	128	256
5×5	150	275

Table 4.5: Trade-off between sub-array size, imaging sequences and number of receiver channels for an $N_{RX} = 256$ array.

Sub-array size	Receiver channels
1	256
4	64
9	28 ($N_{RX} = 252$)
16	16

section and could be seen in Figure 4.5.

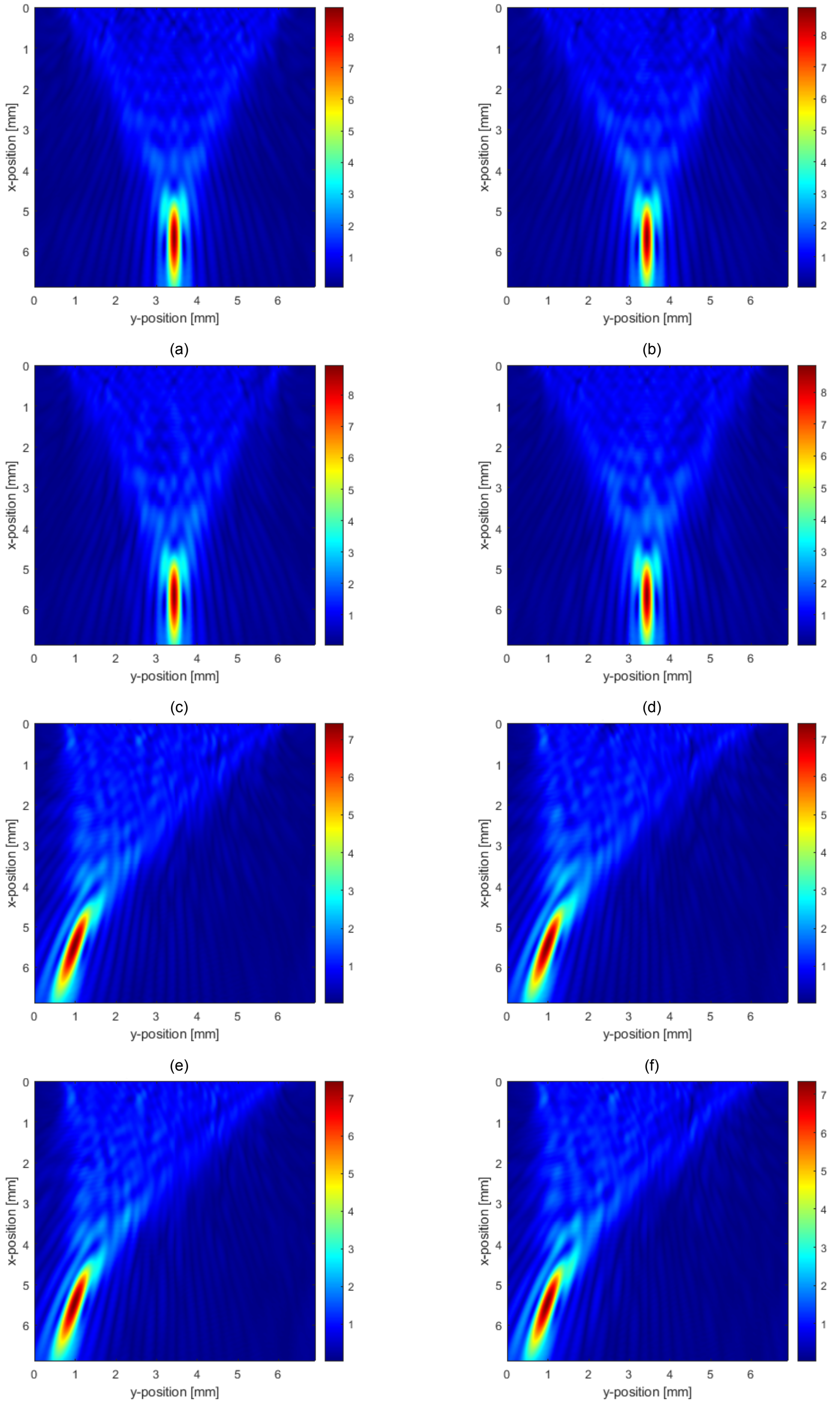

(a) (b)

(c) (d)

(e) (f)

(g) (h)

Figure 4.13: Beam profile for sub-arrays of size 2×2 (a, e), 3×3 (b, f), 4×4 (c, g) and 5×5 (d, h) with a 0° steering angle (a)-(d) and a 20° steering angle (e)-(h). The dimensions of the focal area do not change significantly. The beam profiles of (a)-(d) correspond with the arrays of Figure 4.11(a)-(d), respectively.

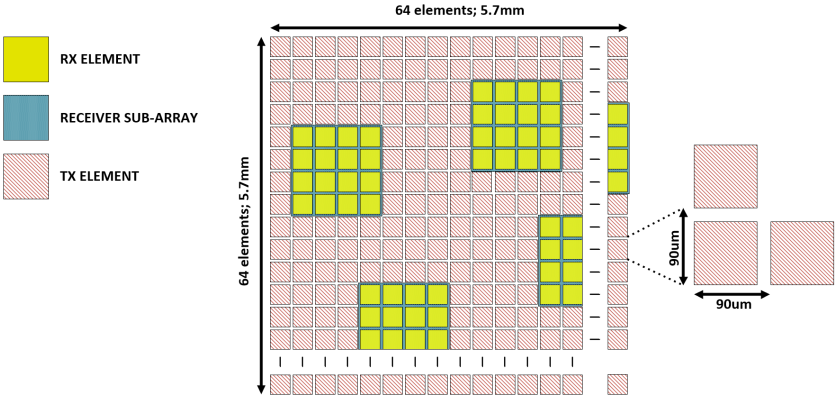

Figure 4.14: Array design using sub-arrays of receive (RX) elements to generate a sparse synthetic receive aperture by multiplexing each element in the sub-array to the receiver chain.

5

Front-End Receiver Design

The receiver AFE is responsible for the signal conditioning, amplification and digitization of the scattered echoes coming from the tissue. The first stage of the AFE consists of a LNA and the CMOS design of this amplifier will be presented in this chapter. A complete receiver front-end has been designed in [12]. That front-end consists of a low-noise amplifier, time-gain compensation amplifier and 6-bit analog-to-digital converter. This thesis does not focus on the CMOS design of the complete signal chain. However, a redesign of the front-end amplifier will be discussed since it comprises a change in amplifier topology. The design is done using the TSMC 180 nm BCD process.

5.1. Transducer Model

The Butterworth-van Dyke lumped-element model for a piezoelectric transducer has been introduced in Section 2.3.1. In this section the parameters will be calculated to be used throughout the design. Since the piezo material has not physically been measured using an impedance analyser, the circuit elements have to be calculated using parameters from the datasheet [34]. Figure 2.4 has been copied to this section into Figure 5.1.

Piezoelectric transducers exhibit a resonance frequency when the motion branch is in series resonance. The impedances of the capacitor C_s and inductor L_s cancel, leaving only resistor R_s at resonance. Another resonance mode, called anti-resonance since it results in a high impedance, is found when the motion branch is in parallel resonance with C_p. The anti-resonance mode arises from the current generated by the piezoelectric effect being out of phase with the current generated by the transducer as a dielectric.

The resonance and anti-resonance frequencies, f_r and f_a respectively, are related via the electromechanical coupling coefficient k_{eff} [36].

$$f_r = f_a\sqrt{1 - k_{eff}^2} \tag{5.1}$$

With a typical $k_{eff} = 0.7$ and $f_r = 8.4$ MHz, the anti-resonance frequency $f_a = 11.8$ MHz. From the two frequencies the element values can be calculated since

$$\begin{aligned} L_s C_s &= \frac{1}{(2\pi f_r)^2} = 360 \times 10^{-18} \\ L_s C_{eq} &= \frac{1}{(2\pi f_a)^2} = 180 \times 10^{-18} \end{aligned} \tag{5.2}$$

with $C_{eq} = C_s C_p/(C_s + C_p)$. This means that $C_s = C_p$ since $C_{eq} = 0.5 C_s$. The capacitance C_p can be calculated using the expression for a parallel plate capacitor $C = \epsilon A/t$.

To calculate the thickness, the speed of sound in the piezo material has to be known. From [36] the sound velocity for length-extension mode transducers can be calculated using the material properties and is given by $v_{piezo} = (\rho s_{33}^D)^{-1/2} = 3850$ m/s. Since the piezo thickness is half of the anti-resonance

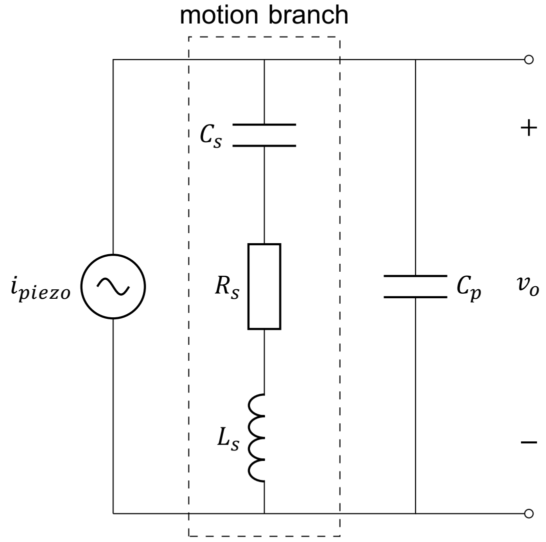

Figure 5.1: Butterworth-Van Dyke model of the piezoelectric transducer (copy of Figure 2.4).

wavelength [35], the thickness is calculated to be

$$t = \frac{(\rho s_{33}^D)^{-1/2}}{2f_a} = 160\,\mu\text{m} \tag{5.3}$$

The capacitances are now calculated to be $C_p = C_s = 0.8\,\text{pF}$. From (5.2) and the calculated C_s, the inductance can be derived and is $L_s = 480\,\mu\text{H}$.

Finally the resistor in the motion branch has to be calculated. Since the mechanical quality factor is known from the datasheet ($Q_m = 32$), the resistance can be calculated using the definition of the Q-factor for a series RLC circuit.

$$R_s = \frac{1}{Q_m}\sqrt{\frac{L_s}{C_s}} \tag{5.4}$$

This results in an $R_s = 800\,\Omega$. The lumped-element component values are summarized in Table 5.1.

For circuit simulations, the piezo transducer is modelled using a single capacitor of 5 pF. This simplifies the design and is a good compromise between having a relatively low impedance at resonance but a capacitive behaviour for frequencies above and below resonance.

5.2. Front-end Requirements

To get an idea for the generated charge, the charge coefficient of the piezoelectric material, d_{33} is used. From the datasheet, $d_{33} = 650\,\text{pC/N}$.

$$Q_{piezo} = d_{33} p_{echo} A \tag{5.5}$$

with p_{echo} the incoming echo pressure and A the area of the transducer element. While the pixel pitch is 90 µm, the dimensions of the piezo transducer are set to 60 × 60 μm^2. This is because the fabrication

Table 5.1: Component values of the used Butterworth-van Dyke piezo model.

Component	Value
C_s	0.8 pF
C_p	0.8 pF
L_s	480 µH
R_s	800 Ω

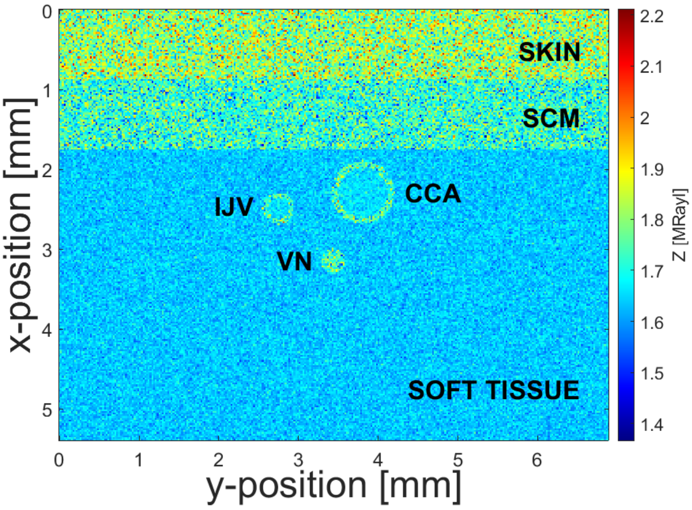

Figure 5.2: Acoustic impedance map of the tissue model including skin, SCM muscle, CCA, IJV and the vagus nerve (VN).

process creates a kerf between the elements due to the dicing process. A dicing kerf of 30 µm is assumed, which is in line with current literature [64].

Since no physical measurements have been performed, a MATLAB simulation has been done to obtain the pressure coming back to the array interface when a plane wave is transmitted with a 200 kPa transmit pressure. To get the most realistic results, a tissue model (based on Figure 1.1) has been used which includes the skin, SCM muscle, CCA, IJV and the vagus nerve (VN). The acoustic impedance map of the model can be seen in Figure 5.2. From the simulation, the RMS pressure at the maximum imaging depth is 500 Pa. To convert this pressure into an equivalent input current, (5.6) is used. Because the signal is assumed to be sinusoidal, the sinusoidal charge distribution of the piezo will create a sinusoidal input current. The current equals the rate of change in the piezo charge. This translates to a charge 'slew rate'. The echo pressures can be seen in Figure 5.3.

$$I_{piezo} = 2\pi F_{res} d_{33} p_{echo} A. \tag{5.6}$$

The minimal Since the depth of interest is very shallow, the difference in pressures coming from different depths small. This means that a TGC amplifier can be omitted.

5.3. Architecture Selection

The piezoelectric transducers generate a charge in response to an applied force. Three methods exist to sense the piezo charge and generate an electrical signal from it. The charge can be sensed by a

1. charge amplifier (CA), by balancing the piezo charge Q_{piezo} with an opposite charge generated by applying a voltage to a feedback capacitor C_f and measuring the voltage $V_{out} = Q_{piezo}/C_f$.
2. voltage amplifier (VA), by sensing the voltage due to the source capacitance $V_{piezo} = Q_{piezo}/C_{piezo}$ directly.
3. transimpedance amplifier (TIA), by sensing the current $I_{piezo} = dQ_{piezo}/dt$ and converting it to an output voltage $V_{out} = I_{piezo}R_f$ through a resistor.

All three methods are used in ultrasound imaging systems. In previous work [12], a capacitive-feedback voltage amplifier is used where the piezo capacitance and the feedback capacitor form an inverting amplifier gain of $A_v = -C_s/C_f$. In this case, the source capacitance was determined to be 5 pF. With a feedback capacitor $C_f = 265$ fF, the voltage gain was set to 25 dB.

The small source capacitance calculated in the previous section makes it difficult to implement this architecture. The minimum metal-insulator-metal (MIM) capacitance available in the process is 33 fF. For the same 25 dB gain, the feedback capacitor should be set to 45 fF. While this capacitance could be layed-out, the process variations for such small values will affect the gain a lot.

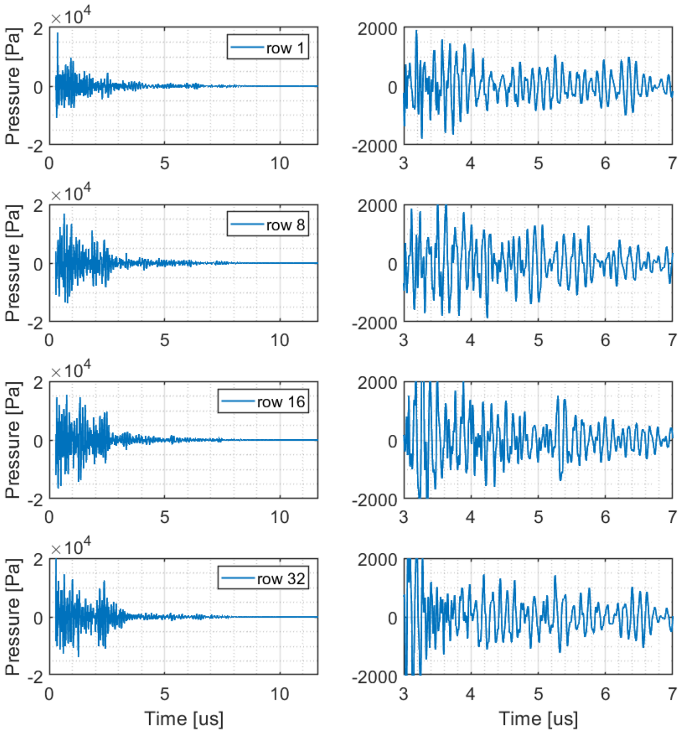

Figure 5.3: Echo pressures coming back to the transducer interface. The echo at four different locations is showed. The right hand side shows a zoomed in view of the pressure at the imaging depth.

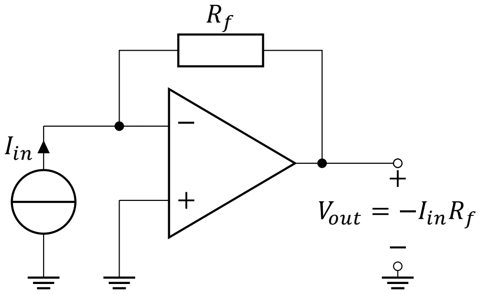

Figure 5.4: Typical transimpedance amplifier architecture based on an operational amplifier with feedback resistor R_F.

In the array design of Section 4.3, the AFE is shared among all elements in the sub-array. This means that the connection from the transducer element to the input of the LNA is different for each element. For a VA, the input capacitance is part of the gain expression (i.e. $V_{out}/V_{in} = -C_{in}/C_F$). The changing distributed capacitance will change the gain for each element.

The small required feedback capacitor together with the variations in input capacitance make the design of a voltage amplifier difficult. Therefore, it is chosen not to use a VA implementation for the front-end. A TIA can be a suitable architecture, since the virtual ground at the inverting input eliminates the influence of any parasitic capacitance connected to this node. The use of the TSMC 180 nm-BCD process allows the use of high-valued resistors with relatively small areas. A TIA is able to provide amplifications of small currents if high valued resistances are used as the feedback resistor. A TIA can be seen in Figure 5.4.

5.3.1. Folded-cascode OTA

Continuing on the work of [12], a folded-cascode operational transconductance amplifier (OTA) topology with N-type metal-oxide-semiconductor (NMOS) input transistors will be used for the opamp in Figure 5.4. Current flowing through the top P-type metal-oxide-semiconductor (PMOS) transistors M4-M5 will be split into the differential pair and folded branch. The largest part of the current will be through the input transistors M1-M2. In order to reduce the power consumption of the amplifier, the supply voltage has been lowered from 1.8 V in [12] to 1.2 V.

The voltage gain of the OTA can be given as the product of the effective transconductance G_m multiplied with the resistance seen at the output of the OTA, see (5.7). Since the input transistors M1-M2 provide the transconductance gain for this amplifier, G_m is approximately equal to their transconductance $g_{m1,2}$.

$$A_v = -G_m R_{out} \approx -g_{m1,2} R_{out} \tag{5.7}$$

The output impedance is improved by the cascode transistors M6-M9. A single transistor has an output resistance given by $r_o = 1/\lambda I_D$, where λ is the channel-length modulation coefficient and I_D the drain current. Cascoding a single common-source stage increases the output resistance by approximately the intrinsic gain of the cascode transistor $g_{m,casc} r_{o,casc}$. The full expression of the output resistance can be given as

$$R_{out} = (1 + g_{m,c} r_{o,c}) r_o + r_{o,c} \approx g_{m,c} r_{o,c} r_o \tag{5.8}$$

with $g_{m,c}$ and $r_{o,c}$ the transconductance and output resistance of the cascode transistor, respectively, and r_o the output resistance of the common-source stage. For the folded-cascode topology, the resistances seen at the PMOS branch and the NMOS branch are in parallel at the output node. This complicates the expression to

$$\begin{aligned} R_{out} &= r_{o,p} || r_{o,n} \quad \text{with} \\ r_{o,p} &= g_{m6,7} r_{o6,7} (r_{o1,2} || r_{o4,5}) \\ r_{o,n} &= g_{m8,9} r_{o8,9} r_{o10,11} \end{aligned} \tag{5.9}$$

It can be seen that to have a high gain, the output resistances and intrinsic gain of the cascodes should be high.

For the TIA to sense a current, the input resistance of the TIA should ideally be zero. This way no current will be wasted in the source. The input transistor provides a infinite input resistance at DC (neglecting gate current), so the feedback resistor is the only element contributing to the finite resistance seen from the source. Negative feedback decreases the input impedance by a factor $(1+A)$ [65]. Thus,

$$R_{in} = \frac{R_f}{1 + A}. \tag{5.10}$$

However, this is assuming the opamp in Figure 5.4 has an ideal zero output resistance. When the input resistance is worked out for the circuit in Figure 5.7, the output impedance r_o of the OTA will appear in the expression

$$R_{in} = \frac{R_f + r_o}{1 + g_m r_o}. \tag{5.11}$$

Looking at (5.7-5.11), a contradiction for the value of R_{out} can be seen. In the numerator of (5.11) R_{out} should be minimized to lower the impedance. However, the gain term $g_m R_{out}$ should be maximized in (5.7) and in the denominator of (5.11) for a low impedance.

A method has to be found to decouple the output impedance from the gain expression [46]. The solution is the implementation of a voltage buffer stage in the form of a source follower shown in Figure 5.5. The buffer does not load the OTA, so the gain can still benefit from the high r_o due to the cascoding. A typical output impedance for a cascoded stage is in the order of 100 kΩ, which is equal to the feedback resistance and thus has a large influence on the transimpedance gain. The source follower (common drain stage) has an output impedance of $R_{out,buf} = 1/g_m$, which is a couple of kΩs. This is two orders of magnitude below the feedback resistance and can therefore be neglected.

In this design, the output of the OTA is connected to a PMOS source follower.The bias current is fixed to 50 μA to limit the power consumption of the buffer. Since a second stage is needed to amplify signal for driving the ADC, the buffer does not need to drive a large load. The small-signal model for the TIA with buffer is seen in Figure 5.8.

Previous work also included a buffer stage behind the front-end amplifier, but that buffer has not been incorporated into the loop. Inside the loop, the common-drain stage can be DC or AC-coupled to the OTA output. Since AC-coupling requires a large capacitance in order to obtain a low-impedance connection, DC-coupling has been used. The low supply voltage of 1.2 V made the implementation

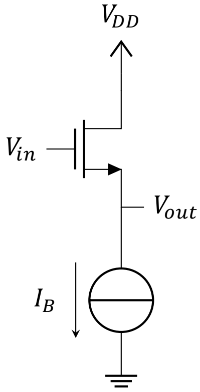

Figure 5.5: Source follower stage with bias current source I_B.

difficult. The gate-source voltage offset from buffer input to output poses strict constraints on the common-mode voltage and OTA output. It has been chosen to set the common-mode voltage to a high level of 1 V. While this balances the buffer biasing transistor to the edge of saturation, a lower voltage has not been possible. With a V_{GS} of 600 mV, the DC output voltage of the OTA is at 400 mV. Any lower would put the transistors M8-M11 out of saturation. The higher common-mode voltage

The input-referred voltage noise of the OTA should be converted to a input-referred current noise since a current input is wanted. Since $R_f \gg R_s$, the voltage noise will be converted to a current through the source resistor.

$$\begin{aligned}\overline{i_{n,in}^2} &= \frac{\overline{v_{n,ota}^2}}{R_s} + 4kT\frac{1}{R_f} \\ &= 4kT\left(\frac{\gamma}{g_m(R_s||R_f)} + \frac{1}{R_f}\right)\end{aligned} \tag{5.12}$$

The last term can be neglected due to the size of R_f.

The input pair transistors M1-M2 will contribute the most towards the input-referred voltage noise. Since the current noise $\overline{i_d^2} = 4kT\gamma g_m$ of the input pair can directly be translated to the input using $\overline{v_n^2} = \overline{i_d^2}/g_m^2$, the transconductance g_m of the input pair should be high to minimize this contribution.

Since the transconductance of the current sources M3, M4-M5 and M10-M11 do not contribute to the amplification of the input signal, their g_m should be minimized. This reduces their contributions to the input-referred noise. The noise coming from the PMOS current source M4-M5 is especially of importance since these transistors carry the most current, and thus are the second major contributor to the noise.

$$g_m = \frac{2I_D}{V_{OD}} \tag{5.13}$$

To minimize the transconductance of the current source, the overdrive voltage $V_{OD} = V_{GS} - V_{TH}$ in (5.13) should be large.

The cascode transistors M6-M9 contribute to the gain of the input signal. Since cascoding increases the output resistance the intrinsic gain of cascodes $g_{m,casc}r_{o,casc}$, a high g_m is wanted. Of course, a reasonable margin has to be left in the overdrive voltage to accommodate signal swings and process variations. The reduction in the supply voltage also complicates this process since less headroom is available in the first place. For the design of the OTA, the overdrive voltages can be found in Table 5.2.

A second factor in the noise performance is the flicker noise. Again, this is mostly due to the input pair M1-M2. Since the flicker noise decreases with an increase in area WL, the input pair is size such that the thermal noise dominates the noise performance.

The input transistors M1-M2 are biased with large current and have a large W/L ratio. This maximizes the g_m of the devices by placing the transistors into weak-inversion. The length is increased

Transistor	I_D [μA]	V_{OD} [mV]	W/L [μm]
M1-M2	200	70	120/0.3
M3	400	120	32/0.25
M4-M5	225	260	15/0.3
M6-M7	25	100	13/0.25
M8-M9	25	100	5/0.25
M10-M11	25	50	30/0.18
M12	50	60	40/0.18
M13	50	60	60/0.18

Table 5.2: Design parameters for the OTA transistors

from the minimal allowable length to increases output impedance. For the output resistance calculation, M1-M2 are in parallel with M4-M5. Therefore, by increasing the length of both transistor pairs, the output impedance remains high. For the input pair this also increases the area, which limits the flicker noise.

The tail current source M3 has to carry the current of the input pair. Often difficulties can arise in keeping the tail transistor in the saturation region. Since the common-mode input voltage is high, this has not been a problem.

The cascode transistors M4-M5 improve the output resistance of the PMOS portion of the folded branch. The parasitic capacitances at the source of M4-M5 introduces an unwanted pole at $p = g_{m,casc}/C_{casc}$. An increase in g_m cannot easily be made by increasing W/L, since that also increases the node capacitance.

The NMOS current source M10-M11 have a low transconductance to decrease its noise contribution. However, since the output node V_{ota} should be at 400 mV, these transistors require a large overdrive. The gate of M10-M11 directly determines the voltage at the opposite node of the output. To reduce the offset voltage, these two voltages should be matched. Since the current through the folded branch is low compared to the differential pair, the noise contribution of M10-M11 will be low anyway.

5.3.2. Loop gain

The OTA will be used as the opamp in Figure 5.4. The closed-loop gain from input current to output voltage can be expressed as [66]

$$Z_T(s) = R_f \left(\frac{1}{1 + sR_fC_f}\right)\left(\frac{L(s)}{1 + L(s)}\right). \tag{5.14}$$

In this equation the first two terms at the right-hand side specify the (ideal) transimpedance gain set by the feedback network. The last term is the servo function which reduces to unity with large enough loop gain $L(s) = A(s)\beta(s)$. Here, $A(s)$ is the gain of the opamp and $\beta(s)$ the feedback factor given by $\beta(s) = Z_s/(Z_s + Z_f)$. The feedback factor reduces to the resistive voltage divider of R_s and R_f at DC. Equation (5.14) shows a trade-off between ideal transimpedance gain $Z_T = R_f$ and bandwidth due to the feedback network.

At resonance, the piezo model reduces to a parallel (R_s || $1/sC_p$), since the impedance of the motion-branch capacitance and inductance cancel. Since the feedback factor at resonance will be 1 kΩ$/($1 kΩ$+$ 100 kΩ $\approx 1/100$, a large $A(s)$ is needed to let the servo function approach unity. In this design the designed DC-gain will be 60 dB. This is a compromise between spending extra power on increasing the loop gain, and having an accurate transimpedance gain.

The small-signal model of Figure 5.4 can be seen in Figure 5.7, where an input and output capacitance is added. The input capacitance is the parallel combination of the source capacitance and parasitic capacitances (including C_{gs}). The transfer of the feedback network from output to input of the

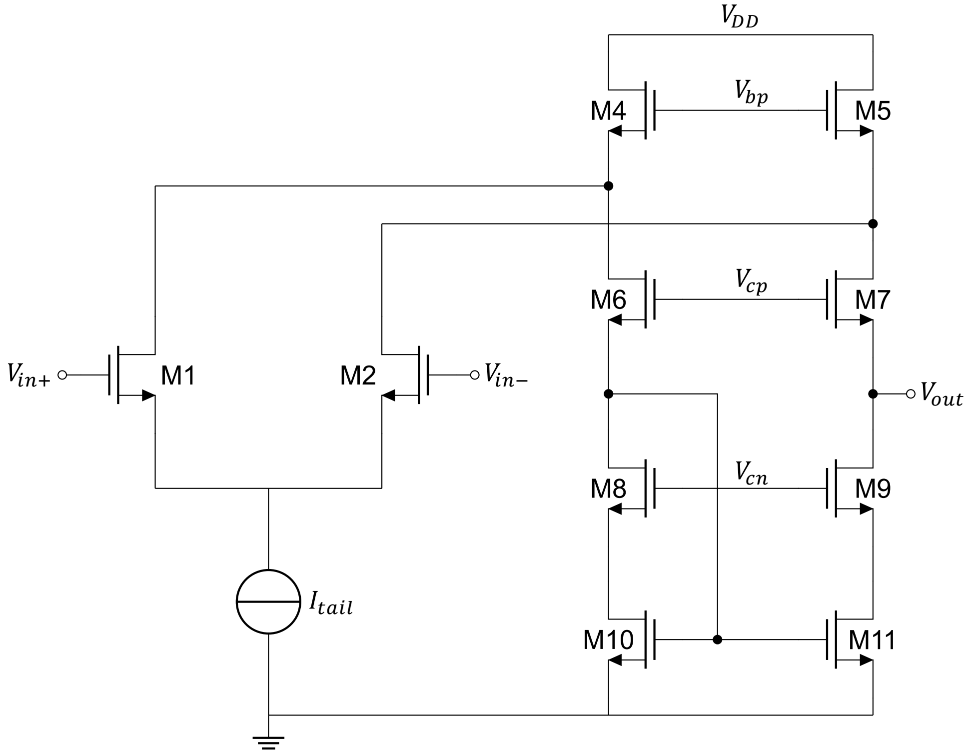

Figure 5.6: Single-ended output folded-cascode OTA topology.

OTA can be given as

$$\begin{aligned}\beta(s) &= \frac{Z_s(s)}{Z_f(s)+Z_s(s)} \\ &= \frac{R_s}{R_s+R_f}\cdot\frac{1}{1+s(R_s||R_f)C_s}\end{aligned} \tag{5.15}$$

with $R_s||R_f$ the parallel combination of R_s and R_f. It can be seen that at DC, the transfer is simply the resistive voltage divider given by the source and feedback resistance. At high frequencies the transfer is dominated by the capacitive division of the feedback and source capacitances. In between these two extremes is a pole.

OTA Frequency Response

The frequency response for the folded-cascode OTA with output buffer can be seen in Figure 5.9(a). While the DC-gain approximately 60 dB, the roll-off is beyond a first-order response and the phase has rotated beyond 180°. This means the amplifier is unstable and frequency compensation has be

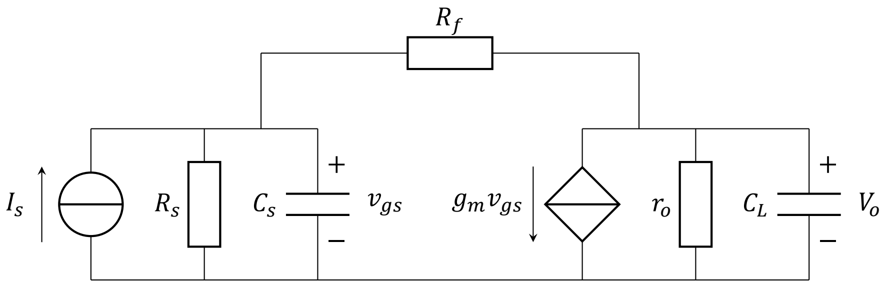

Figure 5.7: Small-signal model of the transimpedance amplifier from Figure 5.4 with added source impedance and load capacitance.

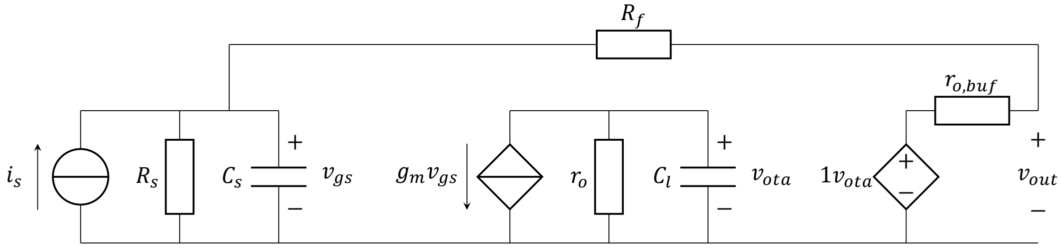

Figure 5.8: Small-signal model of the transimpedance amplifier with added buffer stage (voltage-controlled voltage source).

Parameter	Result
Supply voltage	1.2 V
Total current	500 µA
Power consumption	600 µW
Bandwidth	220 kHz
Input-referred noise	8.4 µV
Phase margin	56°

Table 5.3: Specification of Folded-cascode OTA with Buffer

performed to stabilize it. It can be seen that a dominant pole is present around 100 MHz. This pole can be cancelled if a zero is placed at that frequency.

Since $\beta = 1/100$ at resonance, and using an ideal first-order roll off, the closed-loop bandwidth is 100x the open-loop bandwidth. This is because the gain-bandwidth product is a fixed value. For a closed-loop bandwidth of $f_n = 20$ MHz, the bandwidth of the amplifier need only be 200 kHz.

Since the open-loop bandwidth is sufficient for a closed-loop bandwidth of 20 MHz, frequency compensation can be applied to adjust the response of the amplifier. At the output of the OTA, an series RC shunt is placed. This adjusts the frequency response at two points:

1. The first dominant pole is shifted towards lower frequencies. The pole will move to approximately $p = 1/(r_{o,n}||r_{o,p})C_c$. By selecting a capacitance $C_c = 1.5$ pF and having an OTA output resistance of 360 kΩ according to the simulation, the pole will move to 280 kHz.

2. The zero created by the RC shunt can be place at 100 MHz to cancel the second dominant pole at that frequency. Therefore, the resistance is chosen to be $R_c = 1000\,\Omega$.

The finalized LNA frequency response after compensation can be seen in Figure 5.9(b). The DC gain is 59 dB and the phase margin is improved to 56°. A clear first-order response can be seen with a -3dB bandwidth of 220 kHz. This is in line with the calculations. The simulated parameters can be seen in Table 5.3.

5.3.3. Final TIA

Now that the open-loop response of the LNA is stable with a first-order roll-off, the closed-loop transimpedance response can be simulated. Using a current source input and closing the loop with a feedback resistor of $R_f = 100$ kΩ, the current-to-voltage transfer is simulated and can be seen in Figure 5.10(a). At low frequencies the transimpedance gain $Z_T = 100$ dB due to the feedback resistor. Sharp peaking at 36 MHz occurs and this is unwanted since it will result in long ringing artefacts. By placing feedback capacitor C_f in parallel with R_f, a zero can be created in the loop gain. Properly selecting the value of C_f can place this zero at the peaking frequency.

The feedback capacitor is chosen to be 50 fF. This allows a bandwidth of the TIA of $f_n = 1/(2\pi R_f C_f =$ 30 MHz with a second-order roll-off. While this bandwidth is higher than the

The peaking is due to a pole associated with the source capacitor $C_s = 5$ pF and input resistance $R_{in} = R_f/(1 + A)$.

In previous work the noise efficiency factor (NEF) as a figure-of-merit for the design of the OTA. Since the same folded-cascode topology is used in this design, the NEF is calculated for comparison.

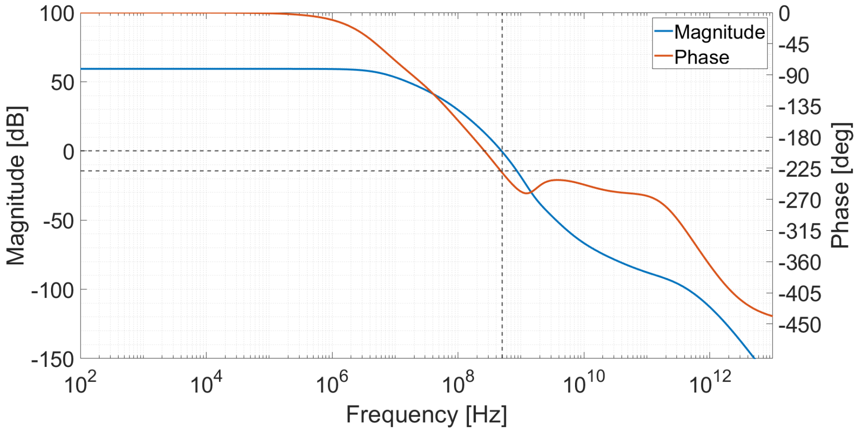

(a)

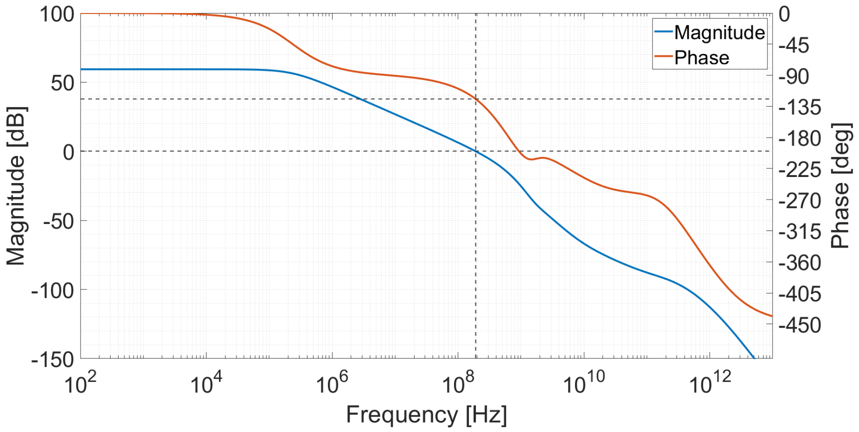

(b)

Figure 5.9: Open-loop frequency response for the OTA with buffer. (a) Uncompensated response, (b) compensated response using RC shunt at OTA output.

The NEF is defined as

$$NEF = V_{ni,rms}\sqrt{\frac{2I_{tot}}{\pi \cdot U_T \cdot 4kT \cdot BW}} \tag{5.16}$$

with $V_{ni,rms}$ the RMS input-referred voltage noise, I_{tot} the total current consumption of the OTA (for comparison the buffer stage is excluded), U_T the thermal voltage taken at 26 mV and BW the noise bandwidth. The calculated $NEF = 3.34$, which is an improvement of the design in [12].

The complete of the LNA with buffer and compensation shunt can be seen in Figure 5.11.

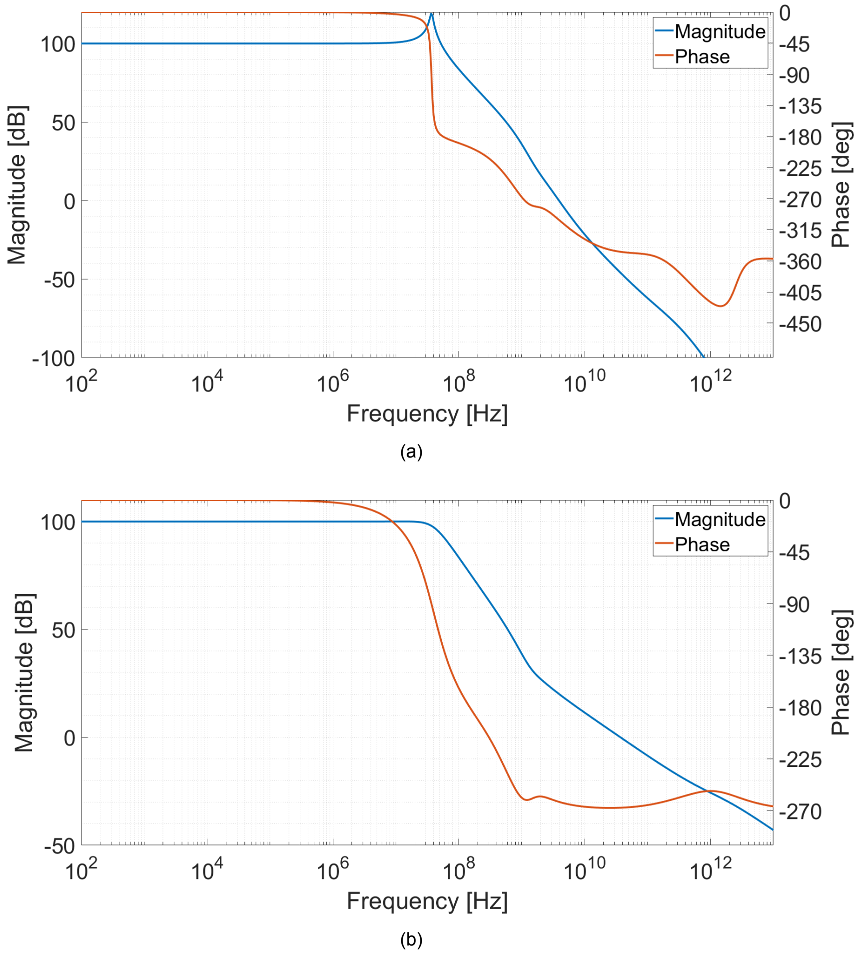

Figure 5.10: Closed-loop transimpedance frequency response for the TIA. (a) Uncompensated response, (b) compensated response using feedback capacitor.

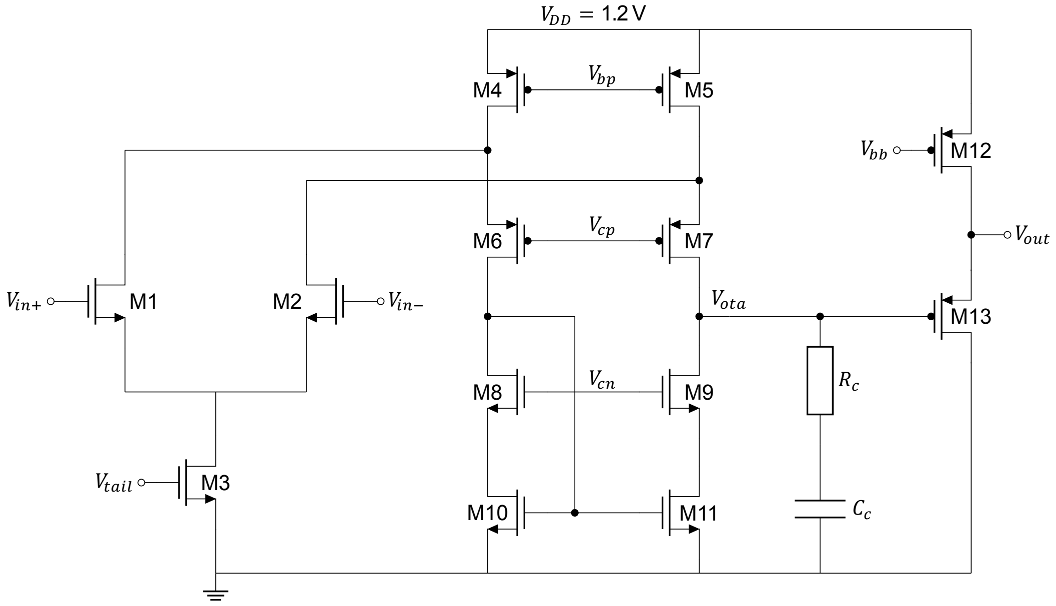

Figure 5.11: Completed folded-cascode OTA topology with output buffer and frequency compensation.

6

Conclusion

In this thesis, the design of an architecture for a wearable vagus nerve stimulation (VNS) was presented. The VNS uses focused ultrasound (FUS) to create a localized high-intensity area at the vagus nerve of mice. By using a 64×64 array at 8.4 MHz, the spatial resolution of the focal area is below 200 µm.

The VNS combines FUS with ultrasound imaging to allow image-guided tracking of the nerve location. This way the high-intensity pressure will always be targeted onto the nerve.

Since the small wavelength of the ultrasound frequency limits the element area, the amount of on-pixel hardware should be minimized. A shared delay-locked loop (DLL) generates the continuous waves for FUS. The transmit pixel only contains two multiplexers, a phase select register and the driver for the transducer. Plane wave imaging (PWI) with a novel inter-element delay specified angles has been used because the delays are fixed and can be generated off-pixel. This shared Column Pulse Control block generates single pulses from the already present DLL phases.

The element area also limits the implementation of the receiver. In this design, 4×4 sub-arrays with shared receivers are sparsely located across the array. The sparse receive aperture will be synthetically generated. The use of PWI minimizes the imaging time so that neuromodulation can continue as long as possible.

Finally, the receiver front-end has been designed in 180 nm CMOS. A transimpedance amplifier (TIA) is used to sense the current coming from the transducer. Since the imaging depth is shallow, the use of a time-gain compensation amplifier is eliminated. Only a fixed gain second stage is needed to interface the TIA with the ADC.

6.1. Thesis Contribution

As mentioned in 1, this thesis is part of the long-term goals on developing a wearable ultrasonic vagus nerve stimulator. My contributions towards this goal are the following:

- Creating the specifications for a wearable VNS.
- Coming up with a novel plane wave imaging scheme based on the existing continuous phases for neuromodulation.
- Combining multiple receive elements into sparsely located sub-arrays for the implementation of a novel synthetic receive aperture imaging scheme.
- The design of a transimpedance front-end amplifier for the elimination of the parasitic capacitances and minimization of the influence of varying source impedance.

6.2. Future Work and Recommendations

Many aspects of this project have not yet been explored or implemented, and many challenges have emerged during the course of this project.
System recommendations:

1. Electrical stimulation has the ability to perform closed-loop neuromodulation. The electrodes can be used for neural recording and the stimulation can be adjusted to the recorded values. Ultrasound cannot be used to read neural activity, so to close the loop other methods have to be found. One method of (indirectly) closing the loop is by using displacement imaging to correlate nerve activation with the displacement of the nerve due to the acoustic radiation force [18].

2. Single-element characterization of a piezoelectric transducer. In Section 5.1 the lumped-element model of the piezoelectric transducer is calculated. The calculation of the element values depend on parameters which, in this thesis, are mostly taken from literature and the data sheet. In practise, many more physical parameters play a role in the properties of the transducers. In order to get the best results, the piezoelectric material should be analysed with an impedance analyzer to obtain the lumped parameters. Next, a test array should be fabricated so that tests can be done on individual elements. This way the most realistic model can be made in order to obtain the specifications of the front-end.

3. For this thesis no physical verification of the different synthetic aperture schemes could be performed. Before implementing this system architecture on an integrated circuit, the various imaging methods should be tested on an ultrasound machine.

Hardware Implementation

1. The scope of this project does not include the implementation of the image reconstruction. As part of the envisioned end-product, the wearable should include an FPGA or microcontroller. For image reconstruction a conventional delay-and-sum algorithm can be used, but it should be optimized for use on a small (i.e. little resources), low-power integrated circuit. Since the image data is only used internally during normal operation, little optimizations on the projection of the image on a display, such as log-compression, are needed.

2. The CMOS design of the front-end amplifier has not been the main goal of this project. A redesign, based on [12] and this work should be done, including the second amplifier stage and ADC.

3. Since the sparse sub-arrays create a large available area for the receiver, it would be possible to implement analog microbeamforming [47] in order to offload the processing power of the FPGA.

4. The large area could also be used to increase the resolution of the ADC. A higher resolution ADC can increase the dynamic range at the input, relaxing the specification for the analog front-end.

5. A folded-cascode topology is not the most power-efficient and noise minimizing topology. A simple inverter stage could be used as the OTA [47].

6. Increasing the number of bits for the DLL could increase the number of plane waves without using larger angles. This could enhance the beamforming process since more pulse-echo sequences can be obtained.

7. The power consumption of the high-voltage driver dominates overall power consumption. The transmit efficiency (defined as the ratio between the acoustic output power and the total dissipated power in the driver circuit and transducer) can be increased by using a multi-level pulser [66].

8. The high-voltage transistors on the TX-pixel occupy a large area. A stacked topology using low-voltage transistors could be implemented [60].

A

Verilog Simulation

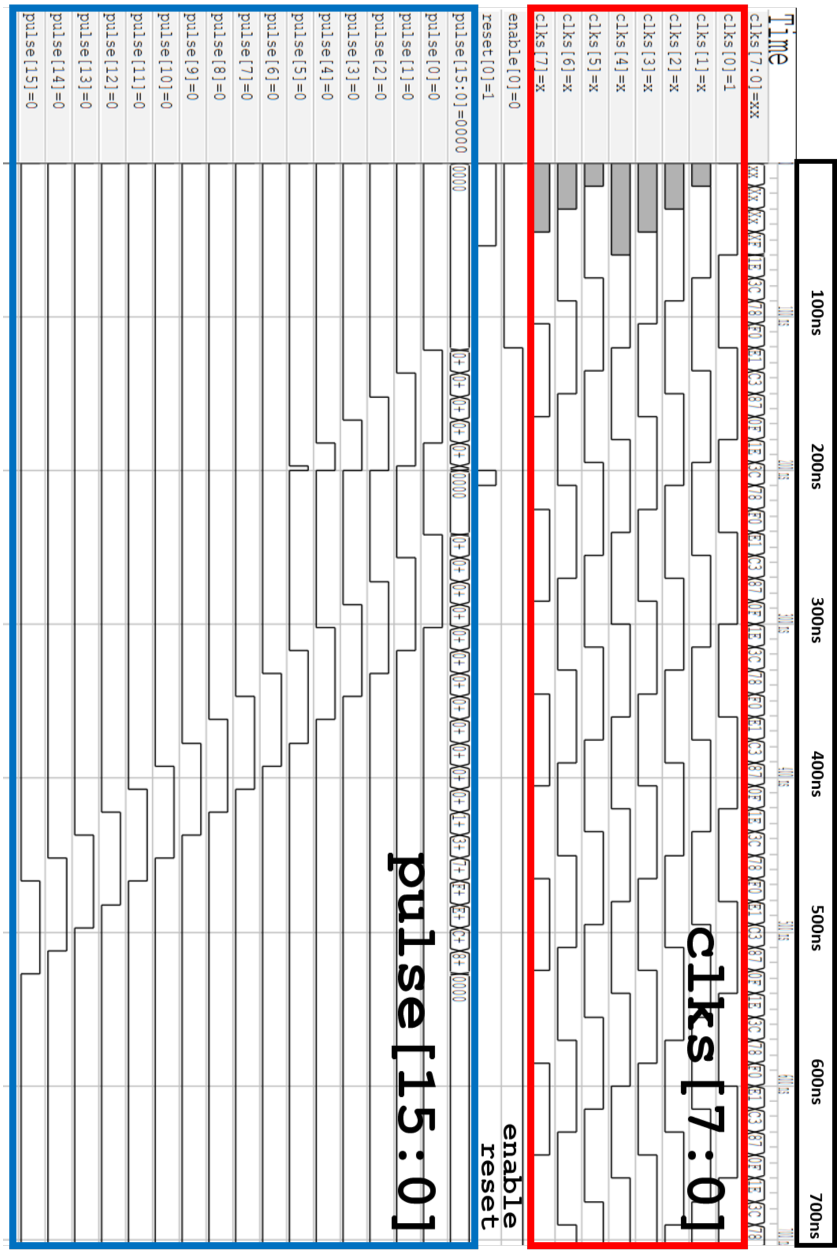

Figure A.1: Simulated Verilog model of the pulse generator. The DLL generates the output phases `clks[7:0]` (in red). Once `enable` is high, the single output pulses can be seen in `pulse[15:0]` (in blue). The pulses will be zero once `reset` is high and, if `reset` is back to low, will resume at the first rising-edge of `clks[0]`.

References

[1] World Health Organization. (Jan. 2021). “Epilepsy Fact Sheet,” [Online]. Available: `https://www.who.int/en/news-room/fact-sheets/detail/epilepsy` (visited on 01/23/2021).

[2] P. Kwan, A. Arzimanoglou, A. T. Berg, M. J. Brodie, W. Allen Hauser, G. Mathern, S. L. Moshé, E. Perucca, S. Wiebe, and J. French, “Definition of drug resistant epilepsy: Consensus proposal by the ad hoc Task Force of the ILAE Commission on Therapeutic Strategies,” *Epilepsia*, vol. 51, no. 6, pp. 1069–1077, Nov. 2009.

[3] R. E. Elliott, A. Morsi, S. P. Kalhorn, J. Marcus, J. Sellin, M. Kang, A. Silverberg, E. Rivera, E. Geller, C. Carlson, O. Devinsky, and W. K. Doyle, “Vagus nerve stimulation in 436 consecutive patients with treatment-resistant epilepsy: Long-term outcomes and predictors of response,” *Epilepsy & Behavior*, vol. 20, no. 1, pp. 57–63, Jan. 2011.

[4] N. Zangiabadi, L. D. Ladino, F. Sina, J. P. Orozco-Hernández, A. Carter, and J. F. Téllez-Zenteno, “Deep Brain Stimulation and Drug-Resistant Epilepsy: A Review of the Literature,” *Frontiers in Neurology*, vol. 10, Jun. 2019.

[5] J. M. Bottomley, C. LeReun, A. Diamantopoulos, S. Mitchell, and B. N. Gaynes, “Vagus nerve stimulation (VNS) therapy in patients with treatment resistant depression: A systematic review and meta-analysis,” *Comprehensive Psychiatry*, vol. 98, p. 152 156, 2020.

[6] F. A. Koopman, S. S. Chavan, S. Miljko, S. Grazio, S. Sokolovic, P. R. Schuurman, A. D. Mehta, Y. A. Levine, M. Faltys, R. Zitnik, K. J. Tracey, and P. P. Tak, “Vagus nerve stimulation inhibits cytokine production and attenuates disease severity in rheumatoid arthritis,” *Proceedings of the National Academy of Sciences*, vol. 113, no. 29, pp. 8284–8289, Jul. 2016.

[7] B. Bonaz, V. Sinniger, D. Hoffmann, D. Clarençon, N. Mathieu, C. Dantzer, L. Vercueil, C. Picq, C. Trocmé, P. Faure, J.-L. Cracowski, and S. Pellissier, “Chronic vagus nerve stimulation in Crohn’s disease: a 6-month follow-up pilot study,” *Neurogastroenterology & Motility*, vol. 28, no. 6, pp. 948–953, Jun. 2016.

[8] Z. Lin, L. Meng, J. Zou, W. Zhou, X. Huang, S. Xue, T. Bian, T. Yuan, L. Niu, Y. Guo, and H. Zheng, “Non-invasive ultrasonic neuromodulation of neuronal excitability for treatment of epilepsy,” *Theranostics*, vol. 10, no. 12, pp. 5514–5526, 2020.

[9] O. Naor, S. Krupa, and S. Shoham, “Ultrasonic neuromodulation,” *Journal of Neural Engineering*, vol. 13, no. 3, p. 031 003, Jun. 2016.

[10] B. Feng, L. Chen, and S. J. Ilham, “A Review on Ultrasonic Neuromodulation of the Peripheral Nervous System: Enhanced or Suppressed Activities?” *Applied Sciences*, vol. 9, no. 8, p. 1637, Apr. 2019.

[11] X. Yang, “Ultrasound Transmitter for Non-invasive Vagus Nerve Stimulation,” Ph.D. dissertation, Delft University of Technology, 2021.

[12] S. Wang, “An ultrasound receiver channel for vagus nerve imaging,” Ph.D. dissertation, Delft University of Technology, 2020, p. 94.

[13] R. Câmara and C. J. Griessenauer, “Chapter 27 - Anatomy of the Vagus Nerve,” in *Nerves and Nerve Injuries*, R. S. Tubbs, E. Rizk, M. M. Shoja, M. Loukas, N. Barbaro, and R. J. Spinner, Eds., vol. 31, San Diego: Academic Press, Jun. 2015, ch. Chapter 27, pp. 385–397.

[14] A. Inamura, S. Nomura, H. Sadahiro, H. Imoto, H. Ishihara, and M. Suzuki, “Topographical features of the vagal nerve at the cervical level in an aging population evaluated by ultrasound,” *Interdisciplinary Neurosurgery: Advanced Techniques and Case Management*, vol. 9, no. June 2015, pp. 64–67, 2017.

[15] A. I. Sonmez, D. D. Camsari, A. L. Nandakumar, J. L. V. Voort, S. Kung, C. P. Lewis, and P. E. Croarkin, “Accelerated tms for depression: A systematic review and meta-analysis,” *Psychiatry Research*, vol. 273, pp. 770–781, 2019.

[16] J. M. Stilling, O. Monchi, F. Amoozegar, and C. T. Debert, “Transcranial magnetic and direct current stimulation (tms/tdcs) for the treatment of headache: A systematic review,” *Headache: The Journal of Head and Face Pain*, vol. 59, no. 3, pp. 339–357, 2019.

[17] S. K. Moore, “Follow the wandering nerve,” *IEEE Spectrum*, vol. 52, no. 6, pp. 78–82, Jun. 2015.

[18] S. A. Lee, H. A. S. Kamimura, and E. E. Konofagou, “Simultaneous Nerve Displacement Mapping for Human Peripheral Neuromodulation,” in *IEEE International Ultrasonics Symposium, IUS*, vol. 2019-Octob, IEEE, Oct. 2019, pp. 2155–2157.

[19] V. Pashaei, P. Dehghanzadeh, G. Enwia, M. Bayat, S. J. A. Majerus, and S. Mandal, “Flexible Body-Conformal Ultrasound Patches for Image-Guided Neuromodulation,” *IEEE Transactions on Biomedical Circuits and Systems*, vol. 14, no. 2, p. 1, Apr. 2020.

[20] E. N. Harvey, “The Effect Of High Frequency Sound Waves On Heart Muscle And Other Irritable Tissues,” *American Journal of Physiology-Legacy Content*, vol. 91, no. 1, pp. 284–290, Dec. 1929.

[21] L. R. Gavrilov, G. V. Gersuni, O. B. Ilyinski, E. M. Tsirulnikov, and E. E. Shchekanov, “A study of reception with the use of focused ultrasound. I. Effects on the skin and deep receptor structures in man,” *Brain Research*, vol. 135, no. 2, pp. 265–277, Oct. 1977.

[22] S. Yoo, D. R. Mittelstein, R. Hurt, J. Lacroix, and M. G. Shapiro, “Focused ultrasound excites neurons via mechanosensitive calcium accumulation and ion channel amplification,” *bioRxiv*, p. 2020.05.19.101196, 2020.

[23] M. D. Menz, P. Ye, K. Firouzi, A. Nikoozadeh, K. B. Pauly, P. Khuri-Yakub, and S. A. Baccus, “Radiation Force as a Physical Mechanism for Ultrasonic Neurostimulation of the Ex Vivo Retina,” *The Journal of Neuroscience*, vol. 39, no. 32, pp. 6251–6264, Aug. 2019.

[24] T. J. Manuel, J. Kusunose, X. Zhan, X. Lv, E. Kang, A. Yang, Z. Xiang, and C. F. Caskey, “Ultrasound neuromodulation depends on pulse repetition frequency and can modulate inhibitory effects of TTX,” *Scientific Reports*, vol. 10, no. 1, p. 15 347, Dec. 2020.

[25] M. Plaksin, S. Shoham, and E. Kimmel, “Intramembrane Cavitation as a Predictive Bio - Piezoelectric Mechanism for Ultrasonic Brain Stimulation,” *Physical Review X*, vol. 4, no. 1, p. 011 004, Jan. 2014.

[26] M. L. Prieto, Ö. Oralkan, B. T. Khuri-Yakub, and M. C. Maduke, “Dynamic Response of Model Lipid Membranes to Ultrasonic Radiation Force,” *PLoS ONE*, vol. 8, no. 10, W. Phillips, Ed., e77115, Oct. 2013.

[27] H. A. S. Kamimura, A. Conti, N. Toschi, and E. E. Konofagou, “Ultrasound Neuromodulation: Mechanisms and the Potential of Multimodal Stimulation for Neuronal Function Assessment,” *Frontiers in Physics*, vol. 8, no. May, pp. 1–9, May 2020.

[28] T. L. Szabo, *Diagnostic Ultrasound Imaging: Inside Out*, 1st ed. Burlington, MA: Elsevier Academic Press, 2004, p. 549.

[29] IT’IS Foundation. (Jan. 2021). “Acoustic Properties,” [Online]. Available: `https://itis.swiss/virtual-population/tissue-properties/database/acoustic-properties/` (visited on 01/27/2021).

[30] K. D. Evans, B. Weiss, and M. Knopp, “High-intensity focused ultrasound (HIFU) for specific therapeutic treatments a literature review,” *Journal of Diagnostic Medical Sonography*, vol. 23, no. 6, pp. 319–327, 2007.

[31] S. Yoshizawa, T. Ikeda, A. Ito, R. Ota, S. Takagi, and Y. Matsumoto, “High intensity focused ultrasound lithotripsy with cavitating microbubbles,” *Medical & Biological Engineering & Computing*, vol. 47, no. 8, pp. 851–860, Aug. 2009.

[32] G. Gurun, C. Tekes, J. Zahorian, T. Xu, S. Satir, M. Karaman, J. Hasler, and F. L. Degertekin, “Single-chip CMUT-on-CMOS front-end system for real-time volumetric IVUS and ICE imaging,” *IEEE Transactions on Ultrasonics, Ferroelectrics, and Frequency Control*, vol. 61, no. 2, pp. 239–250, 2014.

[33] W. D. O’Brien Jr., “Ultrasound–biophysics mechanisms,” *Progress in Biophysics and Molecular Biology*, vol. 93, no. 1-3, pp. 212–255, Jan. 2007.

[34] Piezo.com. (Oct. 2021). “Piezo Material Properties Datasheet,” [Online]. Available: `https://info.piezo.com/hubfs/Data-Sheets/piezo-material-properties-data-sheet-20201112.pdf` (visited on 10/17/2021).

[35] Z. Zhang, J. Xu, L. Yang, S. Liu, J. Xiao, X. Li, X. Wang, and H. Luo, “Design and comparison of PMN-PT single crystals and PZT ceramics based medical phased array ultrasonic transducer,” *Sensors and Actuators, A: Physical*, vol. 283, pp. 273–281, 2018.

[36] M. M. Ghanbari and R. Muller, “Optimizing Volumetric Efficiency and Backscatter Communication in Biosensing Ultrasonic Implants,” *IEEE Transactions on Biomedical Circuits and Systems*, vol. 14, no. 6, pp. 1381–1392, 2020.

[37] K. Brenner, A. S. Ergun, K. Firouzi, M. F. Rasmussen, Q. Stedman, and B. Khuri-Yakub, “Advances in capacitive micromachined ultrasonic transducers,” *Micromachines*, vol. 10, no. 2, pp. 1–27, 2019.

[38] R. Wodnicki, B. Haider, and K. E. Thomenius, “Electronics for Diagnostic Ultrasound,” *Medical Imaging: Principles, Detectors, and Electronics*, pp. 165–220, 2009.

[39] J. Blackmore, S. Shrivastava, J. Sallet, C. R. Butler, and R. O. Cleveland, “Ultrasound Neuromodulation: A Review of Results, Mechanisms and Safety,” *Ultrasound in Medicine & Biology*, vol. 45, no. 7, pp. 1509–1536, Jul. 2019.

[40] D. H. Turnbull and F. S. Foster, “Beam Steering with Pulsed Two-Dimensional Transducer Arrays,” *IEEE Transactions on Ultrasonics, Ferroelectrics, and Frequency Control*, vol. 38, no. 4, pp. 320–333, 1991.

[41] S. I. Nikolov, “Synthetic aperture tissue and flow ultrasound imaging,” Ph.D. dissertation, Technical University of Denmark, 2002.

[42] M. Karaman, P. C. Li, and M. O’Donnell, “Synthetic Aperture Imaging for Small Scale Systems,” *IEEE Transactions on Ultrasonics, Ferroelectrics and Frequency Control*, vol. 42, no. 3, pp. 429–442, 1995.

[43] M. Tanter, J. Bercoff, L. Sandrin, and M. Fink, “Ultrafast compound imaging for 2-D motion vector estimation: application to transient elastography,” *IEEE Transactions on Ultrasonics, Ferroelectrics and Frequency Control*, vol. 49, no. 10, pp. 1363–1374, Oct. 2002.

[44] G. Montaldo, M. Tanter, J. Bercoff, N. Benech, and M. Fink, “Coherent plane-wave compounding for very high frame rate ultrasonography and transient elastography,” *IEEE Transactions on Ultrasonics, Ferroelectrics and Frequency Control*, vol. 56, no. 3, pp. 489–506, Mar. 2009.

[45] S. I. Nikolov, J. Kortbek, and J. A. Jensen, “Practical applications of synthetic aperture imaging,” *Proceedings - IEEE Ultrasonics Symposium*, pp. 350–358, 2010.

[46] C. Chen, E. Noothout, H. J. Vos, J. G. Bosch, M. D. Verweij, N. de Jong, M. A. P. Pertijs, S. B. Raghunathan, Z. Yu, M. Shabanimotlagh, Z. Chen, Z.-Y. Chang, S. Blaak, C. Prins, and J. Ponte, “A Prototype PZT Matrix Transducer With Low-Power Integrated Receive ASIC for 3-D Transesophageal Echocardiography,” *IEEE Transactions on Ultrasonics, Ferroelectrics, and Frequency Control*, vol. 63, no. 1, pp. 47–59, Jan. 2016.

[47] C. Chen, Z. Chen, D. Bera, S. B. Raghunathan, M. Shabanimotlagh, E. Noothout, Z. Y. Chang, J. Ponte, C. Prins, H. J. Vos, J. G. Bosch, M. D. Verweij, N. De Jong, and M. A. Pertijs, “A Front-End ASIC with Receive Sub-array Beamforming Integrated with a 32 × 32 PZT Matrix Transducer for 3-D Transesophageal Echocardiography,” *IEEE Journal of Solid-State Circuits*, vol. 52, no. 4, pp. 994–1006, 2017.

[48] A. Bhuyan, J. W. Choe, B. C. Lee, I. O. Wygant, A. Nikoozadeh, O. Oralkan, and B. T. Khuri-Yakub, “Integrated Circuits for Volumetric Ultrasound Imaging With 2-D CMUT Arrays,” *IEEE Transactions on Biomedical Circuits and Systems*, vol. 7, no. 6, pp. 796–804, Dec. 2013.

[49] G. Lockwood, “Optimizing the Radiation Pattern of Sparse Periodic Two-Dimensional Arrays,” *IEEE Transactions on Ultrasonics, Ferroelectrics and Frequency Control*, vol. 43, no. 3, p. 499, May 1996.

[50] C. Sciallero and A. Trucco, “Wideband 2-D sparse array optimization combined with multiline reception for real-time 3-D medical ultrasound,” *Ultrasonics*, vol. 111, no. May 2020, p. 106 318, 2021.

[51] J. A. Johnson, M. Karaman, and B. T. Khuri-Yakub, “Coherent-array imaging using phased subarrays. Part I: Basic principles,” *IEEE Transactions on Ultrasonics, Ferroelectrics, and Frequency Control*, vol. 52, no. 1, pp. 37–50, 2005.

[52] J. A. Jensen, S. I. Nikolov, K. L. Gammelmark, and M. H. Pedersen, “Synthetic aperture ultrasound imaging,” *Ultrasonics*, vol. 44, no. SUPPL. 2006.

[53] J.-Y. Jeong, J.-S. An, S.-J. Jung, S.-K. Hong, and O.-K. Kwon, “A Low-Power Analog Delay Line Using a Current-Splitting Method for 3-D Ultrasound Imaging Systems,” *IEEE Transactions on Circuits and Systems II: Express Briefs*, vol. 65, no. 7, pp. 829–833, Jul. 2018.

[54] W. J. Huffman, S. Subramaniyan, R. M. Rodriguiz, W. C. Wetsel, W. M. Grill, and N. Terrando, “Modulation of neuroinflammation and memory dysfunction using percutaneous vagus nerve stimulation in mice,” *Brain Stimulation*, vol. 12, no. 1, pp. 19–29, Jan. 2019.

[55] N. Stakenborg, P. J. Gomez□Pinilla, T. J. M. Verlinden, A. M. Wolthuis, A. D’Hoore, R. Farré, P. Herijgers, G. Matteoli, and G. E. Boeckxstaens, “Comparison between the cervical and abdominal vagus nerves in mice, pigs, and humans,” *Neurogastroenterology & Motility*, vol. 32, no. 9, Sep. 2020.

[56] J. Marini and J. Rivenez, “Acoustical fields from rectangular ultrasonic transducers for non-destructive testing and medical diagnosis,” *Ultrasonics*, vol. 12, no. 6, pp. 251–256, Nov. 1974.

[57] E. Kang, M. Tan, J.-s. An, Z.-y. Chang, P. Vince, N. Senegond, T. Mateo, C. Meynier, and M. Pertijs, “23.6 A 2pA/$\sqrt{\text{Hz}}$ Transimpedance Amplifier for Miniature Ultrasound Probes with 36dB Continuous-Time Gain Compensation,” in *2020 IEEE International Solid- State Circuits Conference - (ISSCC)*, IEEE, Feb. 2020, pp. 354–356.

[58] I. Ghosh, “Neuro-Stent: CMOS driving channel for ultrasonic neurovascular stent,” Ph.D. dissertation, Delft University of Technology, 2021, p. 101.

[59] I. O. Wygant, N. S. Jamal, H. J. Lee, A. Nikoozadeh, Ö. Oralkan, M. Karaman, B. T. Khuri-yakub, O. Oralkan, M. Karaman, and B. T. Khuri-Yakub, “An integrated circuit with transmit beamforming flip-chip bonded to a 2-D CMUT array for 3-D ultrasound imaging,” *IEEE Transactions on Ultrasonics, Ferroelectrics, and Frequency Control*, vol. 56, no. 10, pp. 2145–2156, Oct. 2009.

[60] A. Banuaji and H. K. Cha, “A 15-V bidirectional ultrasound interface analog front-end IC for medical imaging using standard CMOS technology,” *IEEE Transactions on Circuits and Systems II: Express Briefs*, vol. 61, no. 8, pp. 604–608, 2014.

[61] G. Lockwood, “Optimizing the Radiation Pattern of Sparse Periodic Linear Arrays,” *IEEE Transactions on Ultrasonics, Ferroelectrics and Frequency Control*, vol. 43, no. 3, p. 499, May 1996.

[62] C. H. Hu, X. C. Xu, J. M. Cannata, J. T. Yen, and K. K. Shung, “Development of a Real-Time, High-Frequency Ultrasound Digital Beamformer for High-Frequency Linear Array Transducers,” *IEEE Transactions on Ultrasonics, Ferroelectrics, and Frequency Control*, vol. 53, no. 2, pp. 317–323, 2006.

[63] M. K. Son, N. J. Sim, and T. D. Chiueh, “A Novel Minimum Variance Beamformer and Its Circuit Design for Ultrasound Beamforming,” *2020 International Symposium on VLSI Design, Automation and Test, VLSI-DAT 2020*, 2020.

[64] T. Costa, C. Shi, K. Tien, J. Elloian, F. A. Cardoso, and K. L. Shepard, “An Integrated 2D Ultrasound Phased Array Transmitter in CMOS With Pixel Pitch-Matched Beamforming,” *IEEE Transactions on Biomedical Circuits and Systems*, vol. 15, no. 4, pp. 731–742, Aug. 2021.

[65] B. Razavi, “The Transimpedance Amplifier [A Circuit for All Seasons],” *IEEE Solid-State Circuits Magazine*, vol. 11, no. 1, pp. 10–97, 2019.

[66] K. Chen, H.-S. Lee, A. P. Chandrakasan, and C. G. Sodini, “Ultrasonic Imaging Transceiver Design for CMUT: A Three-Level 30-Vpp Pulse-Shaping Pulser With Improved Efficiency and a Noise-Optimized Receiver,” *IEEE Journal of Solid-State Circuits*, vol. 48, no. 11, pp. 2734–2745, Nov. 2013.